SEP 11 1997

SANDIA REPORT

SAND97–2135 • UC–705
Unlimited Release
Printed September 1997

RECEIVED
SEP 15 1997
OSTI

Radiation Transport Phenomena and Modeling
Part A: Codes
Part B: Applications and Examples

L. J. Lorence, Jr., D. E. Beutler

PH

DISTRIBUTION OF THIS DOCUMENT IS UNLIMITED

Prepared by
Sandia National Laboratories
Albuquerque, New Mexico 87185 and Livermore, California 94550

Sandia is a multiprogram laboratory operated bySandia Corporation,
a Lockheed Martin Company, for the United States Department of
Energy under Contract DE-AC04-94AL85000.

MASTER

Approved for public release; distribution is unlimited.

Sandia National Laboratories

SF2900Q(8-81)

Issued by Sandia National Laboratories, operated for the United States Department of Energy by Sandia Corporation.

Printed in the United States of America. This report has been reproduced directly from the best available copy.
Available to DOE and DOE contractors from
Office of Scientific and Technical Information
P.O. Box 62
Oak Ridge, TN 37831

Prices available from (615) 576-8401, FTS 626-8401
Available to the public from
National Technical Information Service
U.S. Department of Commerce
5285 Port Royal Rd
Springfield, VA 22161

NTIS price codes
Printed copy: A05
Microfiche copy: A01

SAND97-2135
Unlimited Release
Printed September 1997

Distribution
Category UC–705

Radiation Transport Phenomena and Modeling*

Part A: Codes

L. J. Lorence, Jr.

Part B: Applications with Examples

D. E. Beutler

Simulation Technology Research Department
Sandia National Laboratories
P.O. Box 5800
Albuquerque, NM 87185-1179

Abstract

This report contains the notes from the second session of the 1997 IEEE Nuclear and Space Radiation Effects Conference Short Course on Applying Computer Simulation Tools to Radiation Effects Problems. Part A discusses the physical phenomena modeled in radiation transport codes and various types of algorithmic implementations. Part B gives examples of how these codes can be used to design experiments whose results can be easily analyzed and describes how to calculate quantities of interest for electronic devices.

---

[*] Presented at the 1997 IEEE Nuclear and Space Radiation Effects Conference (July 21-25, 1997, Snowmass, Colorado).

SAND--97-1233C
CONF-970711--10

II. RADIATION TRANSPORT PHENOMENA AND MODELING

PART A: CODES

Leonard J. Lorence
Sandia National Laboratories
P.O. BOX 5800, Mail Stop 1179
Albuquerque, NM 87185-1179

1.0 INTRODUCTION

The need to understand how particle radiation (high-energy photons and electrons) from a variety of sources affects materials and electronics has motivated the development of sophisticated computer codes that describe how radiation with energies from 1.0 keV to 100.0 GeV propagates through matter. Predicting radiation transport is the necessary first step in predicting radiation effects. The radiation transport codes that are described here are general-purpose codes capable of analyzing a variety of radiation environments including those produced by nuclear weapons (x-rays, gamma rays, and neutrons), by sources in space (electrons and ions) and by accelerators (x-rays, gamma rays, and electrons). Applications of these codes include the study of radiation effects on electronics, nuclear medicine (imaging and cancer treatment), and industrial processes (food disinfestation, waste sterilization, manufacturing.)

The radiation transport codes that we will discuss are general in another sense. They can predict how radiation moves through any material of arbitrary composition in either gas, liquid or solid forms.

Our primary focus will be on coupled electron-photon transport codes. We will also briefly discuss proton transport, but will not describe neutron transport codes. Coupled electron-photon transport codes model a radiation cascade in which electrons produce photons and vice versa. This coupling between particles of different types is important for radiation effects. For instance, in an x-ray environment, electrons are produced that drive the response in electronics. In an electron environment, dose due to bremsstrahlung photons can be significant once the source electrons have been stopped.

All coupled electron-photon transport codes are linear codes. By this we mean that: (1) source particles do not interact with each other and (2) the material medium through which the radiation propagates remains constant and unaffected by the radiation. For instance, the second assumption would not be valid if the interaction rate of particles with the medium changed during irradiation because of heating. We will also restrict our discussion to time-independent radiation transport codes. Most radiation transport codes are of this type.

2.0 RADIATION PHYSICS

2.1 INTERACTION COEFFICIENTS

A useful concept in particle radiation transport is the likelihood that an interaction occurs per distance of travel (or per pathlength.) This is the macroscopic cross section, σ, which has units of cm^{-1} [Chilton]. The macroscopic cross section is also known as the linear attenuation coefficient. Each interaction that a particle undergoes with the medium is described by a cross section. Cross sections are energy-dependent, $\sigma(E)$, and will vary with material. The total macroscopic cross section, σ_t, is obtained by combining the macroscopic cross sections of all interactions. The average distance to the next interaction is the mean free path (or mean pathlength), λ, defined as:

$$\lambda = \frac{1}{\sigma_t} \tag{1}$$

Total macroscopic cross sections for high-energy photons (x-rays and γ-rays) in aluminum and lead are compared in Figure 1 (normalized to density, ρ.) Note that photon cross sections vary significantly over energy and material type. For instance, at energies below 100 keV, the cross section for lead is two orders of magnitude greater than that of aluminum.

Electron cross sections are not as strongly dependent on energy and material type as photon cross sections. Total macroscopic cross sections for electrons in aluminum and lead are compared in Figure 2. This cross section differs by only a factor of two between lead and aluminum over the energy range shown. Electron cross sections are also many orders of magnitude greater than those of photons. This means that photons and electrons interact on radically different lengths of scale.

For instance, the mean free path for 1.0 MeV photons in lead is 1.25 cm, but only 3.0 x 10^{-6} cm for 1.0 MeV electrons.

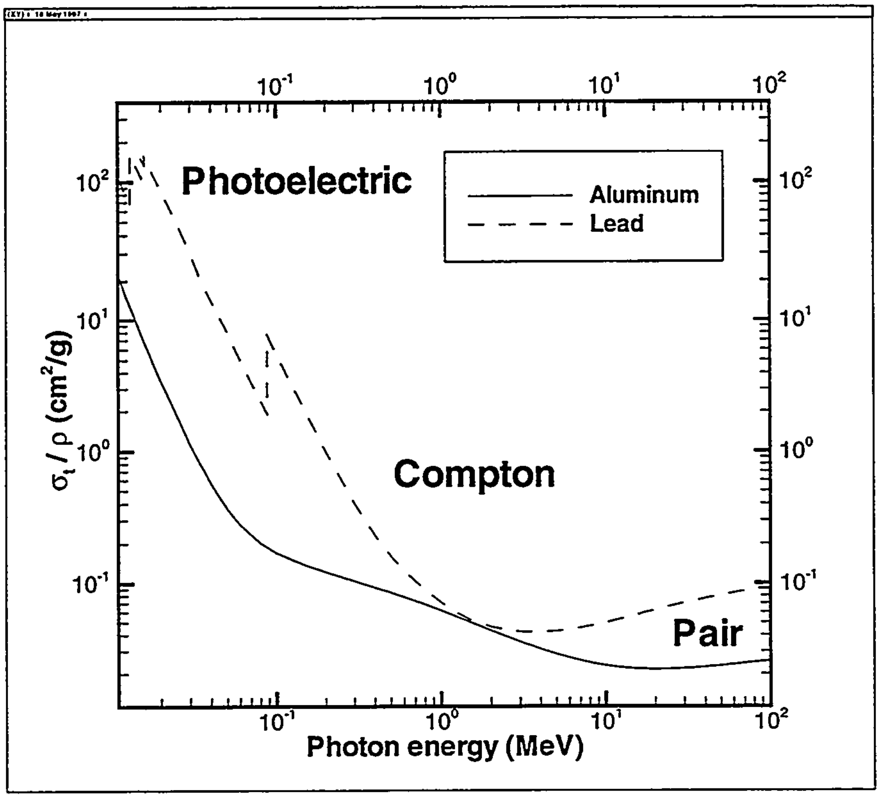

FIGURE 1. Total macroscopic cross section for photons in aluminum and lead

Photon and electron cross sections also undergo significantly different types of interactions. Photon interactions tend to be dominated by absorption events and inelastic scattering events that reduce the energy of the photon significantly. For x-rays, the mean free path roughly indicates the scale of a photon's penetration into a material. A mean free path represents an "*e*-folding" distance for exponential attenuation. That is, over one mean free path, the intensity of a beam of source photons is reduced to e^{-1} (37%) of the original.

Of course, as x-ray radiation penetrates a material, both source radiation that has not yet interacted and photons that have scattered into different energies and/or angles will be present. For instance, for 100 keV x-rays incident on three mean free paths of aluminum and lead, the number of photons transmitted through the material is only about 14% and 12% of the original intensity, respectively. Part of the transmitted radiation consists of the original beam reduced by e^{-3} (5%) of the original intensity.

The mean free path is not a useful measure of the penetrating ability of electrons (or other charged-particles such as protons.) This is because, unlike x-rays, most electron interactions are either elastic (resulting in deflection but no energy-loss) or inelastic with little energy loss. For instance, after 0.03 cm or 10^4 mean free paths, the intensity of a beam of 1.0 MeV electrons in lead is reduced to a few percent of the original. A better measure for penetration depth of electrons is not the mean free path or mean pathlength to the next interaction, but the mean total pathlength traveled by the electron. The mean total pathlength is also known as the continuous-slowing down approximation (CSDA) range.

In order to define the CSDA range, a few other interaction coefficients must be introduced. The first is that of a differential cross section. Differential cross sections specify the likelihood that, per distance of travel, particles will scatter to new energies and angles. For instance, the cross section differential in energy, $\sigma(E \rightarrow E')$, describes the probability that particles scatter from energy E to E' per pathlength traveled.

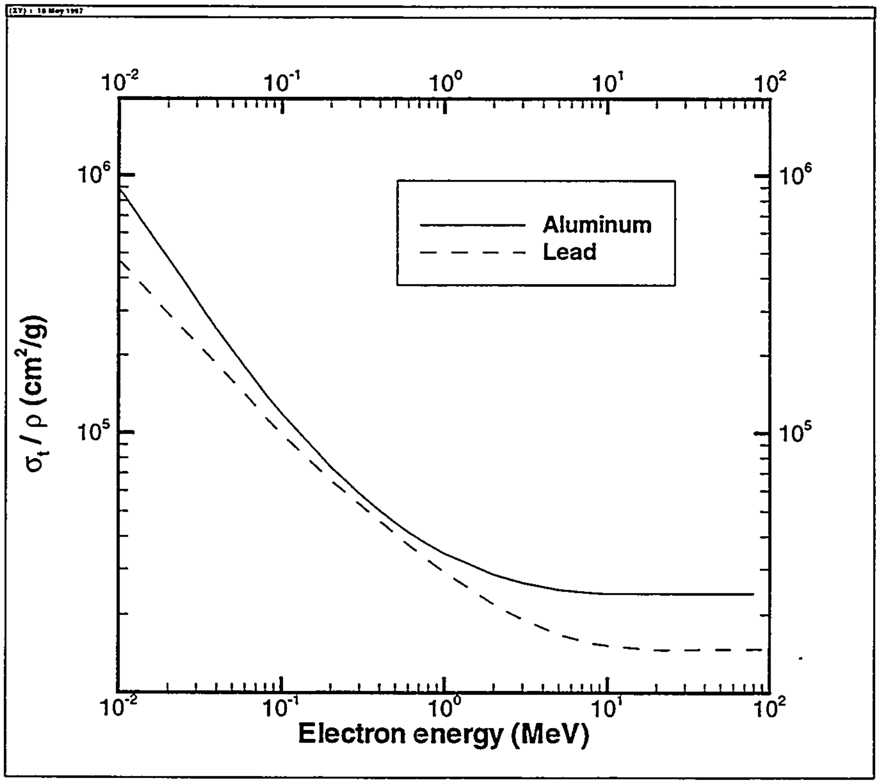

FIGURE 2. Total macroscopic cross section for electrons in aluminum and lead

The cross section differential in energy is defined such that:

$$\sigma(E) = \int_{0}^{\infty} \sigma(E \rightarrow E')\, dE'. \tag{2}$$

Similarly, the cross section differential in angle, $\sigma(\vec{\Omega} \rightarrow \vec{\Omega}')$, describes the probability that particles scatter from angle $\vec{\Omega}$ to angle $\vec{\Omega}'$ per pathlength traveled. Also, the cross section differential in energy and angle, $\sigma(E, \vec{\Omega} \rightarrow E', \vec{\Omega}')$, describes the probability that particles scatter from energy E and angle $\vec{\Omega}$ to energy E' and angle $\vec{\Omega}'$ per pathlength traveled.

A second concept specific to charged particles is the stopping power, defined as the energy loss per pathlength traveled [Attix]. The stopping power has units of MeV/cm. It is obtained from the cross section differential in energy by:

$$S(E) = \int_0^E \varepsilon \sigma (E \rightarrow E - \varepsilon)\, d\varepsilon. \tag{3}$$

Two types of inelastic interactions contribute to the total stopping power of charged particles: collisional and radiative. The latter is associated with the production of bremsstrahlung photon radiation. The collisional stopping powers for electrons in aluminum and lead are shown in Figure 3. The collisional stopping powers are not strongly dependent on material type or energy. An analytical formulation of the collisional stopping power of electrons, protons, and other heavy charged particles was derived by Bethe [Attix]. Evaluation of the Bethe stopping power requires parameters that are generally obtained by experiment and are included in cross-section databases.

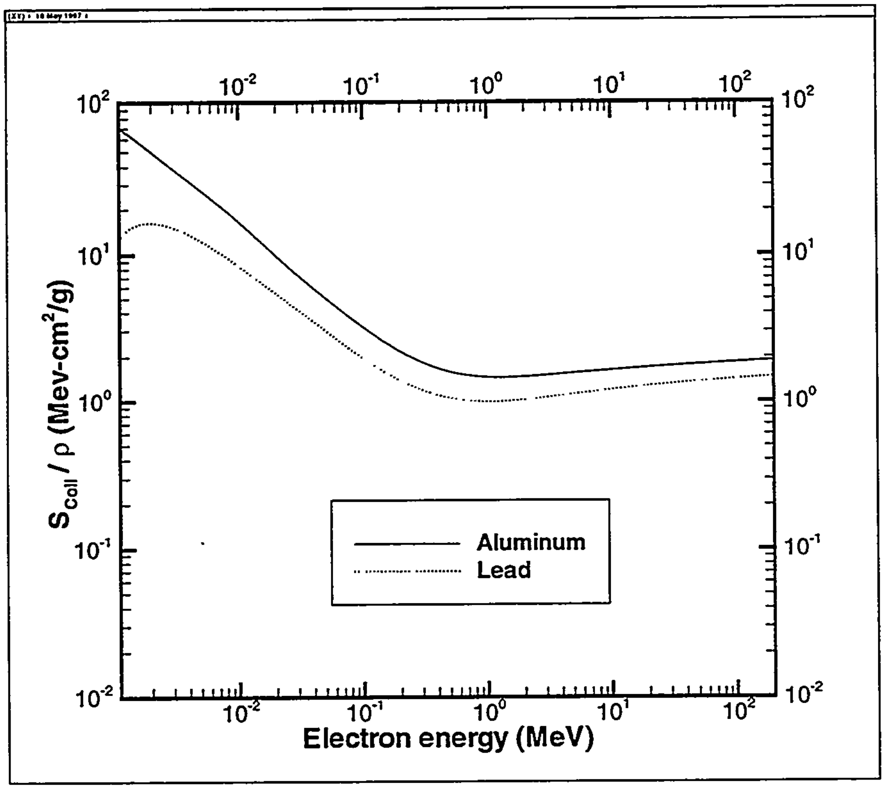

FIGURE 3. Collisional stopping powers for electrons in aluminum and lead

The mean total pathlength or CSDA range of a charged particle with energy, E_{Max}, is related to the stopping power by:

$$Range_{CSDA}(E_{Max}) = \int_{E_{Max}}^{0} \frac{-dE}{S(E)} \quad (4)$$

In a low-atomic-number material, electrons can penetrate close to their CSDA range. This is seen by the depth-dose profile for electrons in a one-dimensional aluminum slab (Figure 4.) The depth-dose profile was calculated with the ITS Monte Carlo transport code [Halbleib] that will be discussed in Section 5.1. The depth-dose curve is normalized to one incident particle per cm^2, a standard normalization in a one-dimensional transport calculation. Also shown are experimental measurements [Lockwood] with about 2% experimental uncertainty.

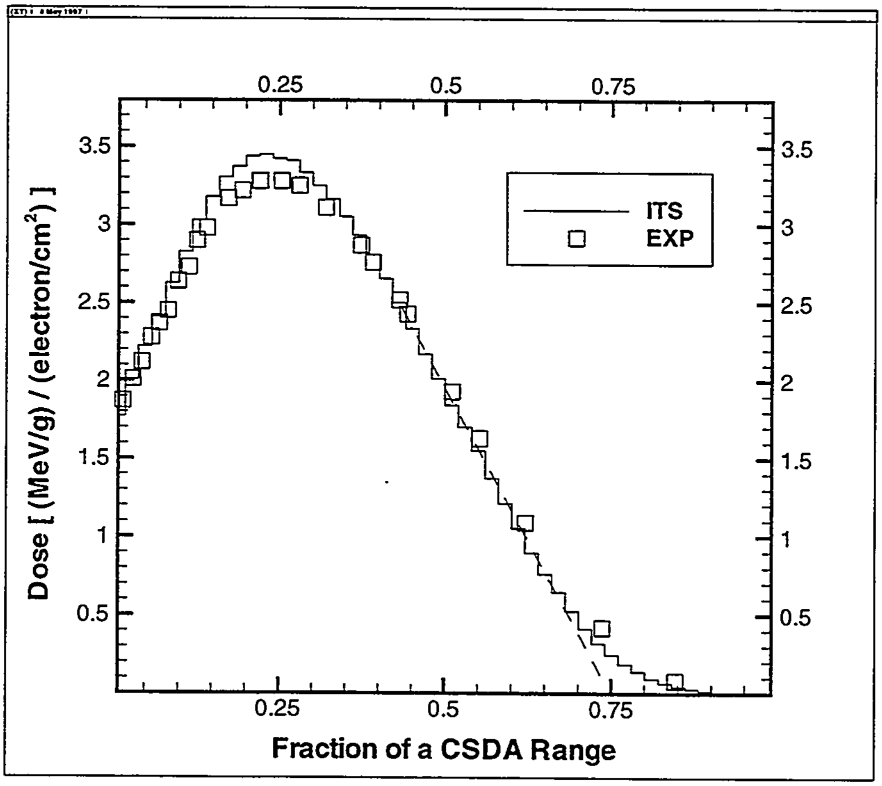

FIGURE 4. Depth-dose curve for 1.0 MeV electrons in aluminum; plane-wave incidence from left

For electrons, a good estimate of maximum penetration distance is the practical or extrapolated range. It is defined by extrapolation from the straight part of the depth-dose profile [Attix]. This is indicated by the dashed line in Figure 4. The ratio of the practical range to the CSDA range is the detour factor, which is approximately constant over a wide energy range. The detour factor in aluminum is about 0.7. Very few electrons (only a few percent) penetrate beyond the practical range. In high-atomic-number materials, deflection due to elastic scattering is more pronounced and causes the detour factor to be much less. Examination of the depth-dose profile for electrons in tantalum (Figure 5) reveals the detour factor to be about half that of aluminum.

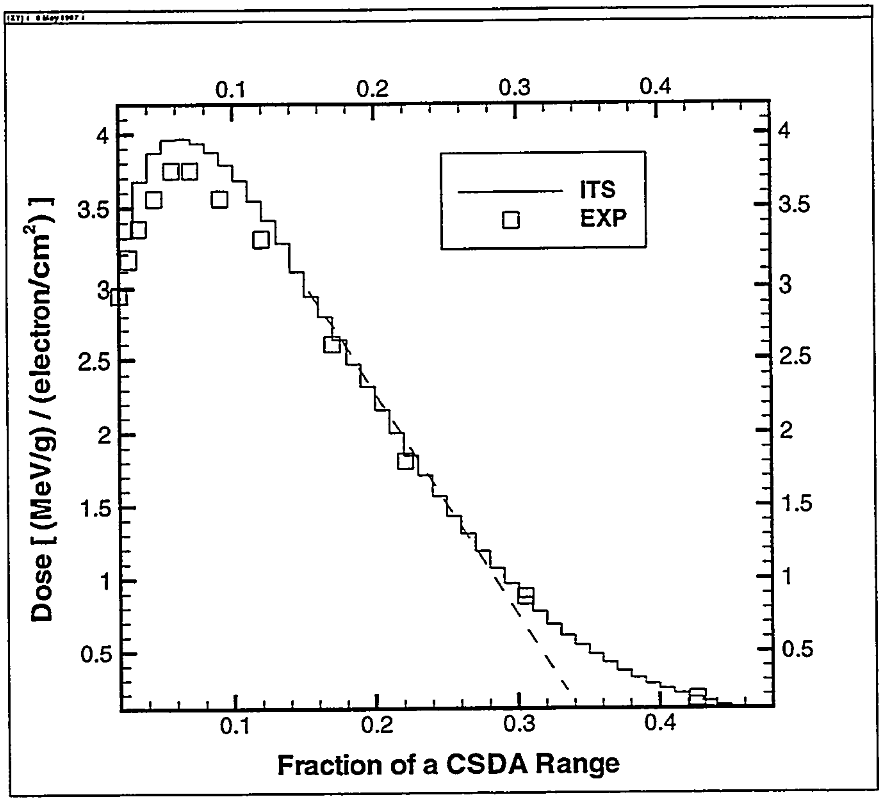

FIGURE 5. Depth-dose curve for 1.0 MeV electrons in tantalum; plane-wave incidence from left

2.2 CROSS-SECTION DATA SETS

In order for radiation transport codes to operate, they must have access to cross section information. For electrons and photons, several databases exit for all elements from Z=1 to 100. The ITS code uses a photon database that was recently devised by the National Institute of Science and Technology (NIST). This database covers the energies from 1.0 keV to 100.0 GeV. Cross-section information is stored at discrete energies and interpolation routines are supplied for efficient sampling of the data. The database allows the macroscopic cross section and cross sections differential in energy and angle for each photon interaction to be reconstructed. Other databases exist that extend photon cross section information down to 10.0 eV [Perkins (a), Biggs]. Generally, photon cross sections are well known over a wide energy range.

A general-purpose radiation transport code needs to assemble cross-section information for arbitrarily-specified materials. For photons, compound cross sections can be readily assembled from elemental cross sections. For instance, an approximation that is generally very good for photons, the Bragg additivity rule, can be applied:

$$\left(\frac{\sigma}{\rho}\right)_{Compound} = \sum_i w_i \left(\frac{\sigma}{\rho}\right)_i \tag{5}$$

This formula specifies that the macroscopic cross section for a compound material (normalized to the density of the compound) is obtained by summing the product of each elemental macroscopic cross section (normalized to the density of the element) with the mass fraction w_i of the element in the compound.

The ITS Monte Carlo code uses a database for electrons that was also devised by NIST. This DATAPAC data set [ICRU] covers the same energy range (and elements) as the NIST photon data set. It allows electron cross sections and other interaction coefficients (stopping powers, ranges, detour factors) to be constructed. For collisional stopping powers, DATAPAC is very accurate above 100.0 keV, with errors on the order of 1-2%. Greater uncertainty exists at lower energies. Between 10.0 and 100.0 keV, stopping powers are estimated to be 2-3% uncertain in low-atomic-number materials and 5-10% uncertain in high-atomic-number materials. The stopping power information from DATAPAC has also been incorporated into other data sets, including one compiled by Livermore National Laboratory [Perkins (b)].

The Livermore data set also contains cross section data for elastic and inelastic electron scattering interactions down to 10.0 eV. However, the data set must be used with caution at low energies. For instance, below 100.0 eV, the uncertainties in the stopping power and elastic scattering data are estimated to be 1000%. Uncertainty in the elemental cross sections is one of the reasons that arbitrary-material electron-photon transport codes such as ITS do not transport electrons below 1.0 keV. However, considerable work has been done to devise specialized techniques and codes for low-energy electron transport in a few select materials, such as silicon and silicon dioxide [Ashley], [Brown], [Woolf].

The construction of arbitrary-material cross sections is also more problematic for electrons than it is for photons. For electrons, the Bragg additivity rule is a poorer approximation and must be supplemented by additional theory and/or experimental data. Such methods have been developed for energetic electrons (energies greater than 1.0 keV.) However, at lower energies, theories do not exist that allow cross sections for compounds of arbitrary composition to be constructed. At these low energies, a variety of solid state phenomena such as plasmon excitation and interaction with conduction band electrons would also have to be modeled.

For protons and other ions, extensive stopping power data sets exist [Anderson], [Janni].

2.3 COUPLED ELECTRON-PHOTON INTERACTIONS

Whether the source of radiation consists of electrons or photons, radiation transport in materials gives rise to a cascade of electrons (e^-), photons (γ), and (possibly) positrons (e^+). For protons, the radiation cascade is not as tightly coupled (i.e. secondary protons are not generated). However, energetic secondary neutrons can be produced by protons and can be important in satellite shielding calculations.

For high-energy photons (x-rays and gamma rays), there are four major types of interactions: photoelectric absorption, incoherent (Compton) scattering, coherent scattering, and pair absorption [Davisson]. In addition, a complex cascade of relaxation radiation (Auger electrons and fluorescence photons) is produced from the atomic transitions that follow photoelectric ionization of atomic shells [Colbert]. High-energy photon interactions are summarized in Table 1

Photoelectric absorption is important below 100.0 keV. Photoelectric cross sections are very sensitive to material type and are greatest in high-atomic-number materials. Photoelectric interactions predominately ionize the inner shells of an atom. For instance, if the photon's energy exceeds the K-shell binding energy, most photoelectric interactions occur with this innermost shell. In high-energy radiation transport codes, only fluorescence photons and Auger electrons greater than 1.0 keV are modelled. Such energetic relaxation radiation is associated with ionization of the innermost atomic shells.

TABLE 1. High-energy photon interactions

Interaction	Cascade	Comment
Photoelectric	γ to e^-,	Absorption of photon
	Relaxation γ and e^-	Photo-electron production
		Ionization of inner atomic shells (photon energy must exceed binding energy of the shell that is ionized)
		Energetic relaxation radiation (> 1.0 keV) that follows this ionization is modelled
Incoherent	γ to γ, e^-	Inelastic photon scattering
		Production of recoil electrons
		Relaxation radiation is low in energy (< 1.0 keV) and is ignored in radiation transport codes
Coherent	γ to γ	Elastic scattering
Pair	γ to e^-, e^+	Absorption of photon. (photon energy must exceed 1.022 MeV)
		Production of an electron and a positron.

The macroscopic cross section for incoherent interactions is approximately independent of material type when normalized to density. This is evident in Figure 1 in the energy regime where incoherent interactions dominate (around 1.0 MeV.) If atomic binding energies are neglected, incoherent interactions can be represented by the Compton process [Attix] in which a photon interacts with a "free" or unbound electron. For greater accuracy, radiation transport codes typically modify the Compton cross section to include the effects of binding energy.

Incoherent photon interactions are scattering events in which the x-ray loses energy and changes direction. In addition, a "recoil" electron is knocked loose from the atom and joins the particle cascade. Ionization primarily occurs in the outermost atomic shells. The cascade of Auger electrons and fluorescence photons that follow ionization of these outer shells is very low in energy (< 1.0 keV). High-energy radiation transport codes ignore the low-energy relaxation radiation generated by incoherent interactions.

Pair absorption occur when photon energy is above the threshold energy that is equivalent to two electron rest masses (about 1.022 MeV). In such interactions, the photon is absorbed and replaced by an energetic electron and a positron which also join the radiation cascade. Coherent photon interactions are elastic scattering events that change a photon's direction without altering the energy of the particle. Such interactions become significant at lower energies (< 100 keV).

For high-energy electrons, there are three major types of interactions: elastic scattering, collisional inelastic scattering, and radiative inelastic scattering [Zerby]. In some radiation transport codes, collisional scattering is further divided into two types: "hard" and "soft." The characteristics of electron interactions are summarized in Table 2.

Unlike the case for photons, elastic interactions for electrons are significant and play a major role in the transport of these particles. Electron elastic interactions are highly-forward peaked (highly anisotropic), especially in low-atomic-number materials. The collisional interactions that ionize the innermost shells result in the greatest energy losses and are known as "hard" or "catastrophic" collisions. Secondary or "knock-on" electrons are also generated and join the particle cascade. In addition, like photo-ionization, collisional events that ionize the innermost shells give rise to a complex cascade of relaxation radiation (Auger electrons and fluorescence photons.)

TABLE 2. High-energy electron interactions

Interaction	Cascade	Comment
Elastic Scattering	e^- to e^-	Highly forward-peaked or anisotropic scattering
Collisional Scattering with Ionization of Inner Shells; "Hard Inelastic"	e^- to e^-, e^-, Relaxation γ and e^-	Inelastic scattering Production of secondary electrons (knock-ons) Ionization of innermost shells leading to relaxation radiation
Collisional Scattering with Ionization of Outer Shells and/or Excitation: "Soft Inelastic"	e^- to e^-	Inelastic scattering. Knock-on electrons and relaxation radiation are very low in energy (< 1.0 keV) and are ignored in high-energy radiation transport codes
Radiative Scattering	e^- to γ, e^-	Inelastic scattering Production of bremsstrahlung photons

The collisional interactions that ionize the outermost shells and/or excite the atom result in the smallest energy losses and are known as "soft." Knock-on electrons and relaxation radiation associated with these interactions are low in energy and are not transported in higher-energy transport codes that cut off particle transport at 1.0 keV.

3.0 PARTICLE RADIATION TRANSPORT

3.1 TRANSPORT EQUATIONS

One way to describe how particles move through materials is through the particle flux, $\psi(r, E, \vec{\Omega})$. The particle flux is the product of particle number density (#/cm^3) and particle velocity. The number density is a distribution that describes the average number of particles in a differential volume about the position, r, a differential energy extent about the energy, E, and a differential angular extent about the angle, $\vec{\Omega}$. From the particle flux, it is possible to extract a variety of information including x-ray spectrum and electron currents. The particle flux can also be used together with cross sections to calculate dose and charge deposition.

The particle flux can be obtained by solving a differential transport equation. The most rigorous transport equation is the three-dimensional time-independent Boltzmann equation [Bell]. With source terms absent, the Boltzmann equation can be written as:

$$\vec{\Omega} \times \nabla\psi + \sigma_t \psi = \iint \sigma(r, E', \vec{\Omega}' \rightarrow E, \vec{\Omega})\, \psi d\vec{\Omega}' dE' \qquad \textbf{(6)}$$

We will not discuss the terms in this differential equation in detail other than to note that the cross section differential in energy and angle appears (to denote material dependence, the cross section is specified as a function of position, *r*.) For coupled electron-photon transport codes, this cross section describes how the energy and the angle of a particle changes (and how secondary electron and photon radiation is produced) as a result of the interactions described in Tables 1-2. For charged particles, other terms that describe the presence of external electromagnetic fields could be added to the Boltzmann equation.

The Boltzmann transport equation is a linear equation. It describes particle transport within a static medium, e.g. the cross sections do not change during the transport. Other non-linearities, such as the interaction of the particles with each other or events that require the simultaneous interaction of two particles with an atom, occur only at very high radiation intensities that are not relevant for most radiation effects. Electromagnetic fields that are self generated by the electron flux are also ignored.

3.2 ELECTRON TRANSPORT

Electron cross sections differ radically from photon cross sections in three respects, all of which tend to complicate the construction and operation of charged-particle transport codes. First, electron cross sections are very large in magnitude. Second, the inelastic scattering cross section differential in energy increases in magnitude as energy loss diminishes. In other words, soft collisions are much more probable than hard collisions. Finally, the elastic scattering cross section is much more significant for electrons than it is for photons. This cross section differential in angle is extremely anisotropic (greatest in magnitude for scattering events that are forward peaked.)

These properties of the electron cross sections make the numerical solution of the electron Boltzmann transport equation difficult. Specialized numerical techniques for electron transport have been devised. In these techniques, aggregate changes in energy and angle of the electron that result from multiple interactions are obtained. Of course, multiple interaction theories are not valid for transport in very thin material layers (on the order of an electron mean free path) where few interactions occur.

The large magnitude of the electron cross sections can be gauged by comparing the macroscopic cross sections for electrons and photons in Figures 1-2. For instance, at 100.0 keV in aluminum, the electron cross sections are about six orders of magnitude greater the photon cross sections. As shown in Figure 6, the cross section differential in energy becomes largest for "soft" inelastic collisions that involve the least transfer of energy. Similarly, the cross section differential in angle becomes largest for those interactions that are involve the least deflection.

Soft collisions are generally chosen to represent interactions that result in energy losses that are a few percent of the electron's energy. In Figure 6, the minimum energy loss in a hard collision has been selected to be 5% of the electron's initial energy.

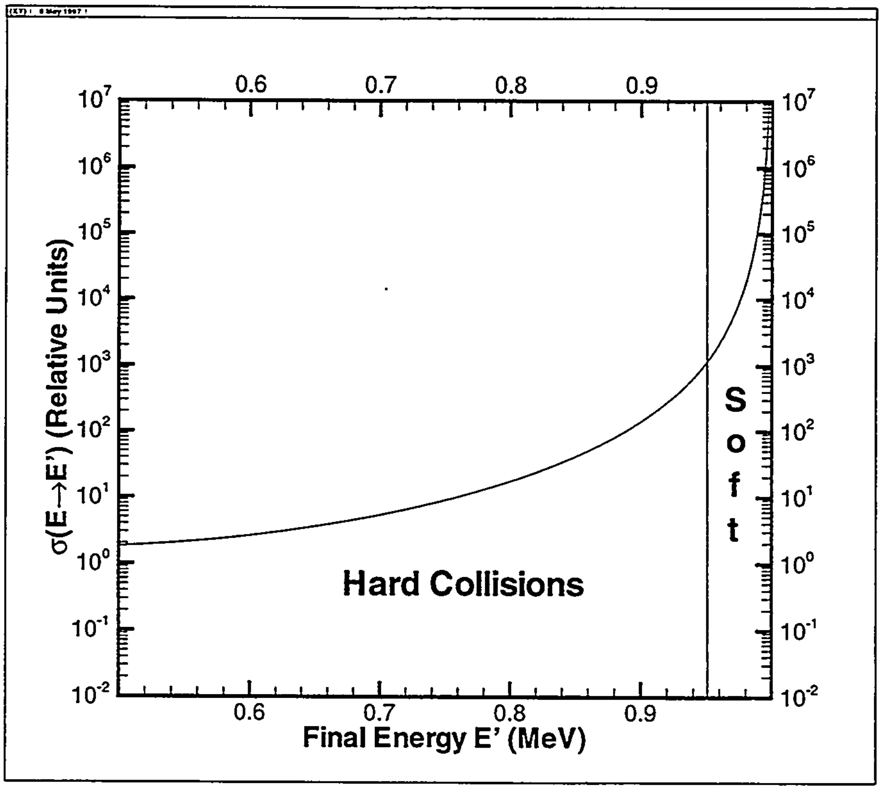

FIGURE 6. Collisional cross section for a 1.0 MeV electron interacting with a single atomic electron

One way to tackle the large magnitude of the inelastic collisional cross section is the continuous slowing down approximation (CSDA). In this approach, many interactions combine to cause a particle to lose energy continuously without deflection. If elastic scattering is neglected <u>and</u>

all inelastic interactions are modelled by CSDA, the electron flux satisfies the CSD transport equation:

$$\vec{\Omega} \times \nabla \psi + \sigma_a \psi = \frac{d}{dE}[S(E)\psi] \tag{7}$$

in which particles lose energy continuously at a rate equal to the stopping power:

$$\frac{dE}{ds} = -S(E) \tag{8}$$

where the pathlength is denoted by the variable, s. Deflections from scattering do not occur. Note that the only cross section that appears in the CSD transport equation is an absorption cross section:

$$\sigma_a = \delta(E - E_{cut}) \tag{9}$$

This cross section accounts for particles which slow down below the cutoff energy, E_{cut}, and are effectively "absorbed".

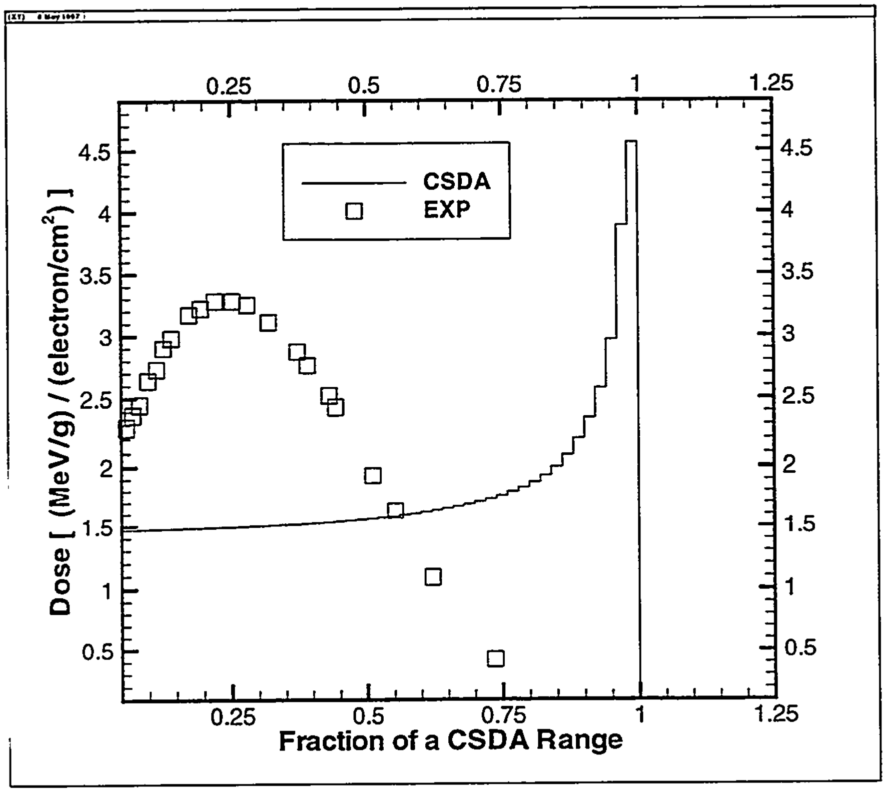

FIGURE 7. Dose-depth profiles for 1.0 Mev electron normally incident (from the left) on an aluminum slab; CSD transport equation

Consider the depth-dose profile of an electron whose transport is governed by the CSD transport equation (Figure 7.) At any point on this profile, all electrons have the same energy and the energy deposition corresponds to the magnitude of the stopping power of these electrons. For instance, at the boundary of the slab where the electrons are incident, the dose is identical to the stopping power of the source electrons. As particles penetrate deeper into the slab, they lose energy and their stopping power increases (see Figure 3), which accounts for the increasing energy deposition.

Without scattering, all particles have the same total pathlength which is equivalent to the distance of penetration. All particles reach the cutoff energy at the same distance, the CSDA range. At this location, the remaining electron energy is deposited and a peak in the profile results. This so-called Bragg peak is a characteristic feature of ion or proton transport. However, although the CSD transport equation is suitable for ion transport, it is does not model electron transport accurately, as indicated by the comparison with experimental data in Figure 7.

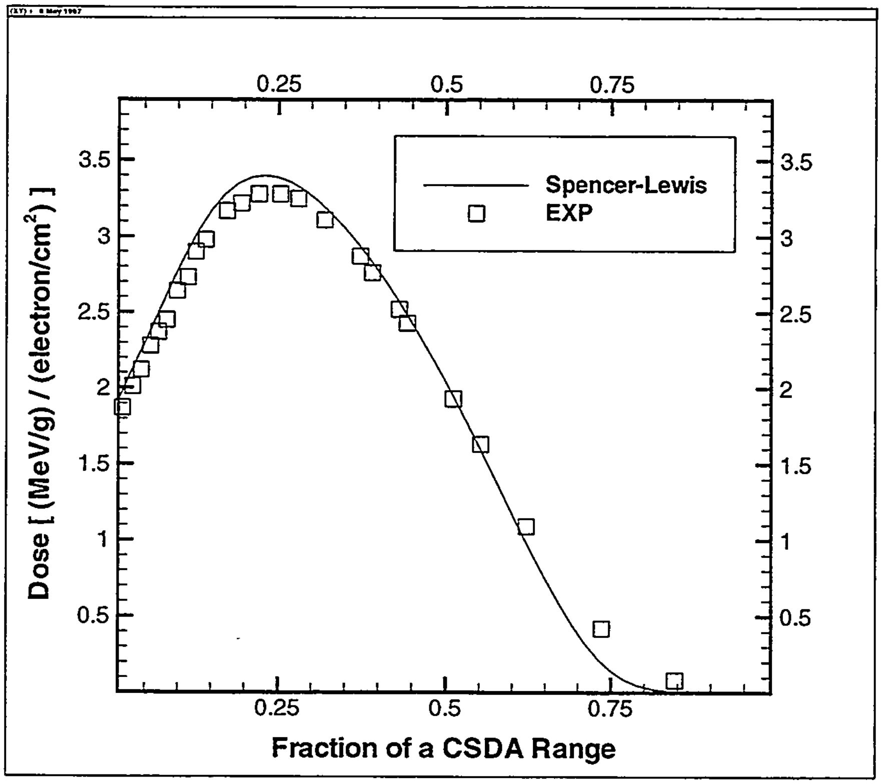

FIGURE 8. Dose-depth profiles for 1.0 Mev electron normally incident (from the left) on an aluminum slab; Spencer-Lewis transport

If elastic scattering is included, a better transport equation for the electron flux is obtained. This is a form of the Spencer-Lewis transport equation [Filippone (a)]:

$$\vec{\Omega}\times\nabla\psi+\sigma_t\psi = \int\sigma_{elastic}(r,\vec{\Omega}'\rightarrow\vec{\Omega})\,\psi d\vec{\Omega}'+\frac{d}{dE}[S(E)\,\psi] \qquad \textbf{(10)}$$

The distinguishing features of Spencer-Lewis transport is that the elastic scattering cross section differential in angle appears explicitly. CSDA is applied for the inelastic interactions.

Because of elastic scattering, particle deflections occur. Hence, pathlength is not equivalent to distance of penetration, as it was for Equation 7. However, all electrons continue to have the same total pathlength, which is equivalent to the CSDA range

For electrons, the depth-dose curve generated by solving the Spencer-Lewis transport equation agrees much more reasonably with experimental data as shown in Figure 8. For instance, peak dose is predicted within 4% (experimental uncertainty is about 2% [Lockwood].) The only significant disagreement occurs in the vicinity of maximum penetration where the solution of the Spencer-Lewis equation underpredicts the dose by 50% or more. This difference reflects the fact that real-world electrons do not all have same total pathlength. The physics that accounts for a distribution of total pathlengths is known as "energy-loss straggling." The absence of energy-loss straggling is a consequence of the absence of the cross section differential in energy in Equation 10.

Since the cross section differential in energy is present in the Boltzmann transport equation, energy-loss straggling is properly represented in the electron flux obtained from this equation. However, because of the large magnitude electron cross sections, the Boltzmann transport equation is not amenable to numerical solution for electrons.

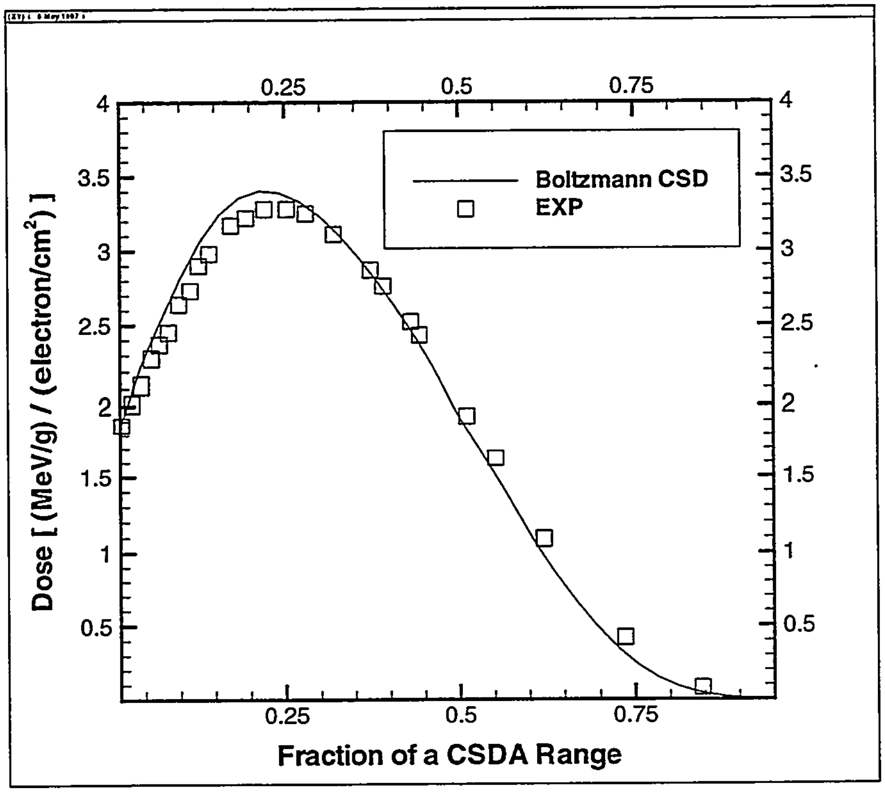

FIGURE 9. Dose-depth profiles for 1.0 Mev electron normally incident (from the left) on an aluminum slab; Boltzmann-CSD transport

One way of substantially restoring energy-loss straggling is to restrict CSDA to soft inelastic collisions only. The Boltzmann-CSD transport equation that results has the following form:

$$\vec{\Omega} \times \nabla\psi + \tilde{\sigma}_t \psi = \int\int \tilde{\sigma}(r, E'\vec{\Omega}' \rightarrow E, \vec{\Omega})\, \psi d\vec{\Omega}' dE' + \frac{d}{dE}[R(E)\psi] \qquad \textbf{(11)}$$

where the "tilde" over the cross sections indicates that soft collisions are excluded. The right side of Equation 11 also includes the restricted stopping power, which is defined only for soft collisions:

$$R(E) = \int_0^{\varepsilon_{Min}} \varepsilon\sigma(E \rightarrow E - \varepsilon)\, d\varepsilon \qquad \textbf{(12)}$$

The salient feature of the Boltzmann-CSD transport equation is that the only macroscopic cross section absent from this equation is the one for soft collisions. Since these interactions are represented by CSDA, energy-loss straggling is ignored for soft collisions. However, since hard collisions result in a distribution of total pathlengths (the average of which is the CSDA range), energy-loss straggling is significantly restored compared to the electron flux obtained from the Spencer-Lewis equation. As shown in Figure 9, the dose-depth profile near maximum penetration is improved.

We will not discuss here how electron transport codes overcome the problem posed by the highly anisotropic form of the elastic scattering cross section. Suffice to say that multiple scattering theories are employed. These methods effectively reduce the elastic cross section and make it much less anisotropic.

3.3 APPROXIMATIONS

One approximation that is common for photon source problems is to simplify the particle cascade by ignoring the transport of electrons altogether. In this approach, the electrons are assumed to deposit their energy locally. If the photon energy is sufficiently high for pair absorption to occur, the electron and positron are assumed to annihilate at the interaction site.

The advantage of ignoring electrons is that it is relatively easy to solve the Boltzmann transport equation for photons. The disadvantage of a photon-only transport code is that electron transport effects are ignored. For instance, charge-deposition and electron currents cannot be calculated with such a code.

A photon-only transport code also cannot predict how energy is redistributed by electron transport. For instance, as shown in Figure 10, electron transport is needed to accurately predict dose in the vicinity of a material interface between high- and low-atomic number materials. Note that, without electron transport, the dose in the silicon layer is underpredicted at the material boundary. This "dose-enhancement" phenomenon involves the redistribution of energy from the higher-atomic-number material to the lower-atomic-number material.

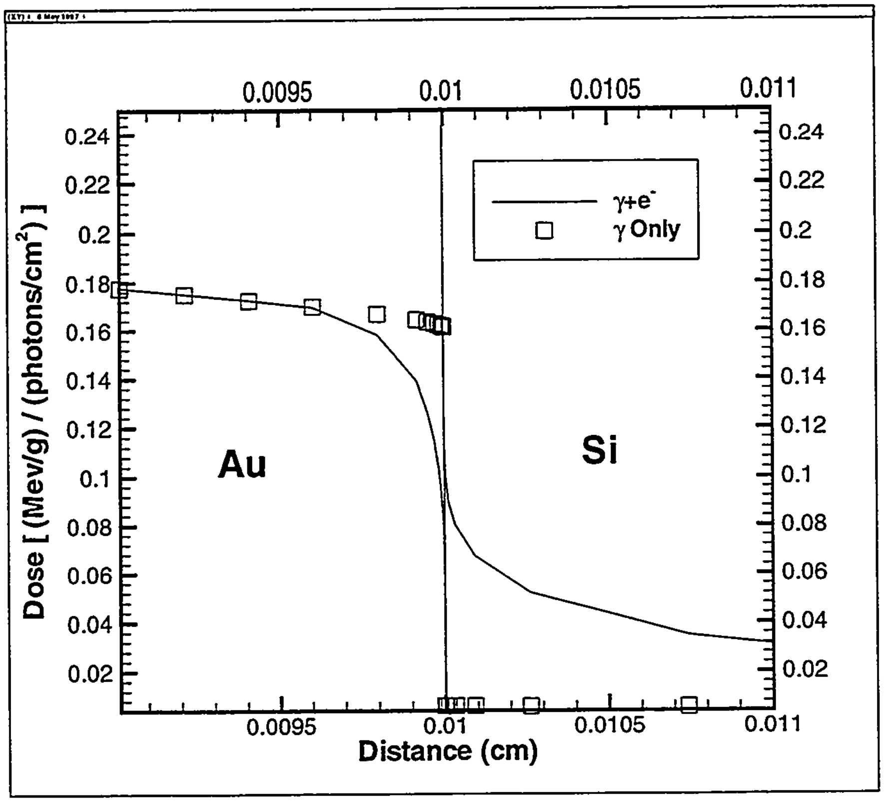

FIGURE 10. Dose-depth profiles at a material boundary for 100.0 keV photons normally incident (from the left) on 0.01 cm layer of gold followed by a 1.0 cm layer of silicon

However, beyond an electron range from material interfaces, the dose will depend only on the photon flux. This is a region of charged-particle equilibrium [Attix]. The dose in such a region can be accurately calculated by photon-only transport and is often referred to as equilibrium dose.

It should be mentioned that non-transport techniques have also been developed. These approximate methods are tailored for specialized applications. Approximate non-transport algorithms, table look-up schemes, and/or extrapolation from previously-calculated transport data are employed. These methods provide ways to obtain information quickly, without a rigorous transport solution, for some classes of problems. A few of these codes are listed in Table 3.

TABLE 3. Non-transport techniques

Code	Source	Application	Method
PHOTCOEF	AIC Software [AIC]	1D x-ray and gamma-ray energy deposition	1D; Exponential attenuation of photons with build-up to account for scattering; Semi-empirical treatment of dose enhancement
QUICKE	Sandia National Laboratories [Dellin] (multiple versions exist in industry)]	1D x-ray photo-Compton electron currents, dose and charge for photon sources	1D; Exponential attenuation of photons, Analytical solution of Spencer-Lewis transport equation, no secondary electron production

TABLE 3. Non-transport techniques

Code	Source	Application	Method
SHIELDOSE	National Institute of Science and Technology [Seltzer]	1D shielding for electron and proton sources with material homogenization	1D; Combination of pre-calculated 1D depth-dose data in aluminum. All materials represented by aluminum-equivalent areal density (the product of density and layer thickness)
SANDOSE	Sandia National Laboratories [Turner]	3D shielding for electron and proton sources with material homogenization	3D; Mass-sectoring analysis using pre-calculated 1D depth-dose data in aluminum. For this 1D data, all materials represented by aluminum-equivalent areal density)

4.0 NUMERICAL TRANSPORT TECHNIQUES

4.1 MONTE CARLO

The Monte Carlo technique is a computational experiment in which individual particle trajectories are simulated by “random walk”. This analog method recreates on a computer only a few of the source particle trajectories or histories that would occur in a real-world experiment. Unlike deterministic codes, Monte Carlo codes do not explicitly solve a transport equation.

A particle history is constructed through systematic sampling of changes in position, energy, and direction using probability distributions derived from cross sections. Various output quantities are obtained, along with their corresponding statistical uncertainties. Typically, Monte Carlo codes normalize all output quantities to one in-coming source particle.

The dominant source of uncertainty in a Monte Carlo calculation is statistical. The usual method of estimating the statistical uncertainty is to divide the total number of histories equally into a reasonably large number of separate computational experiments or “batches”. A statistical analysis is then performed on the spread of the batch results to estimate the statistical uncertainty.

TABLE 4. Average number of elastic collisions which an electron undergoes while slowing down from energy E to 1.0 keV in aluminum and gold

E (keV)	Aluminum	Gold
1024	14820	27380
512	8468	14880
256	4655	7764
128	2557	3912
64	1401	1916

All production coupled electron-photon Monte Carlo transport codes simulate each single photon interaction and employ some form of multiple interaction or “condensed-history” random walk for electrons. In multiple-interaction theories, individual collisions are combined to determine aggregate changes in energy and/or direction. This is done because the number of individual interactions for electrons is huge, as shown in Table 4 [Jenkins]

In a condensed-history electron Monte Carlo, each trajectory is modeled by rectilinear segments. In each segment, the effects of very many individual collisions is obtained by sampling energy losses and deflections from multiple interaction theories. These theories and their implementation can be a distinguishing feature of a code or group of codes.

As an example, consider the main features of the method employed in so-called Class-1 Monte Carlo codes [Berger(b)] such as ETRAN [Berger(a)] and its derivatives: ITS [Halbleib], SANDYL [Colbert], and the electron version of MCNP [Briesmeister]. The distinguishing feature of Class-1 condensed-history is that CSDA with the total stopping power is combined with energy-loss straggling, which is obtained from a multiple-interaction theory. Rectilinear segments (steps) are optimized for determining energy loss. These steps are further divided into substeps to account for angular deflections from multiple elastic and inelastic interactions.

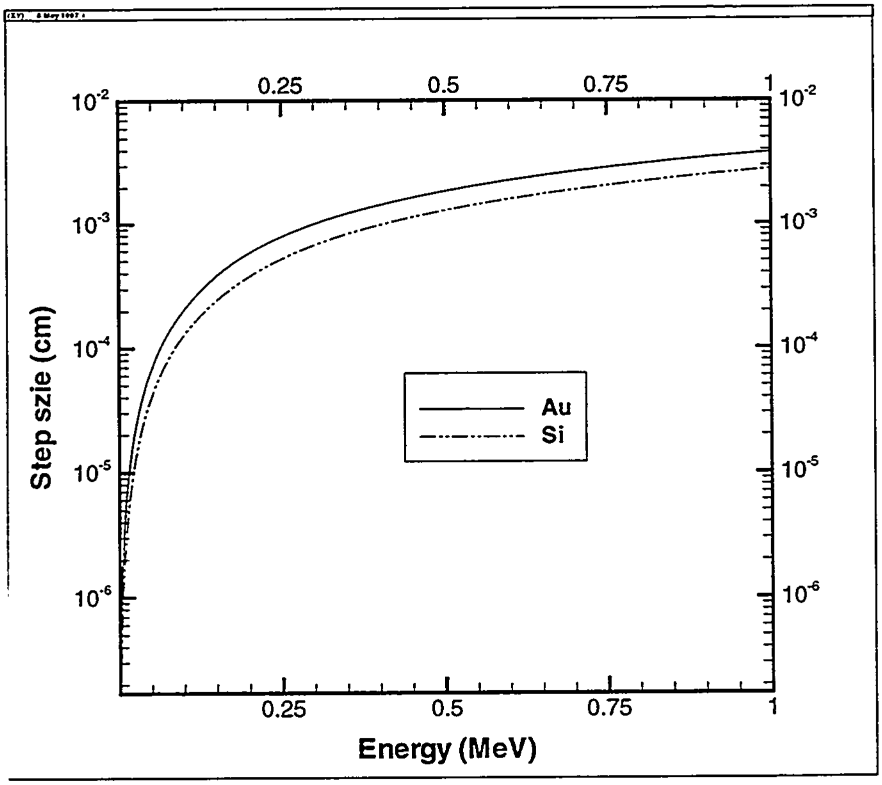

FIGURE 11. Default step sizes from the ITS Monte Carlo code for gold and silicon.

A Monte Carlo random walk of a Class-1 code proceeds in the following manner. Over each step, collisional energy loss is sampled from a condensed-history energy-loss distribution which explicitly accounts for energy-loss straggling. The mean energy loss over a step is the CSDA energy loss. The default step size in ITS for gold and silicon is shown in Figure 11.

Each step is further divided into substeps. Angular deflection is sampled at the end of each substep from another condensed-history distribution. The number of substeps per step is material dependent. For gold and silicon, each step is divided into thirteen and five substeps, respectively. Substeps are much larger than the electron mean free path. Such condensed-history Monte Carlo codes are not expected to be accurate in very thin zones in which substep sizes exceed material layer dimensions.

Secondary particle production (e.g., knock-on and bremsstrahlung) is also sampled within each substep. The energy of the electron at the end of the step depends on both the collisional and radiative losses that have occurred. The random walk then continues with a new step based on this new energy.

In the Monte Carlo code, ITS, defaults exist for all numerical parameters. The parameter that a user is most likely to vary is the number of particle histories. The number of histories can be increased to reduce statistical uncertainties. As the number of particle histories is increased from N_0 to N, the statistical uncertainty is reduced by: $\sqrt{\frac{N_0}{N}}$.

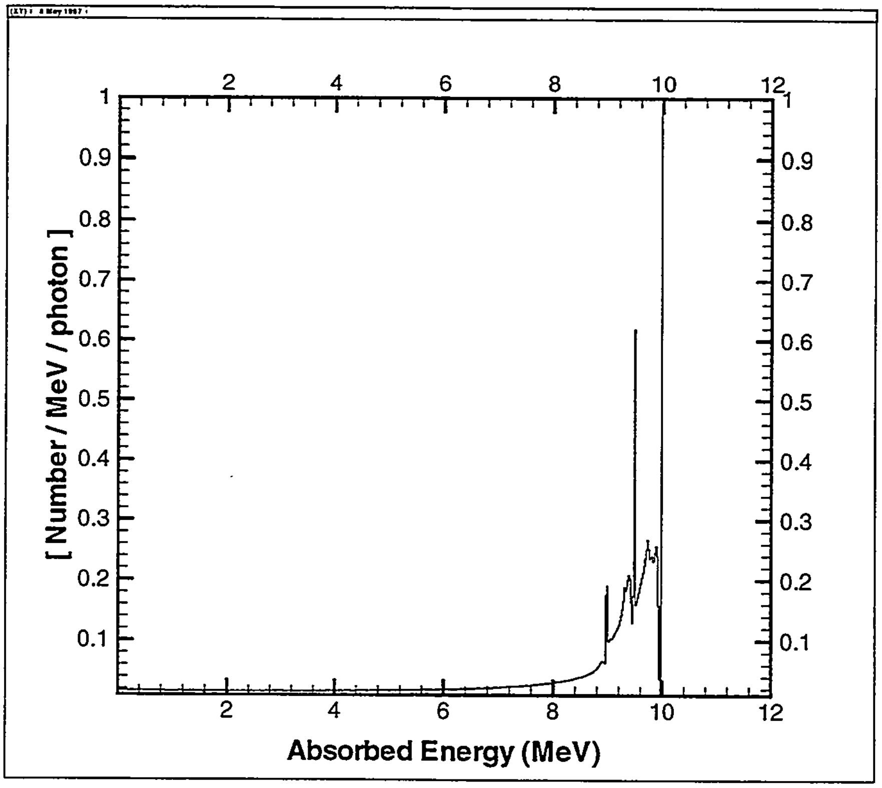

FIGURE 12. Spectrum of absorbed energy for 10.0 MeV photons incident on 8.0 cm of aluminum; Monte Carlo calculation

Monte Carlo codes have a number of inherent advantages over deterministic codes. One significant advantage is that deterministic codes only solve for the particle flux. Monte Carlo codes can provide other kinds of information. Indeed, analog simulation of particle trajectories permits the user to ask virtually any question about how the transport unfolds. For instance, the spectrum of absorbed energy or "pulse-height distribution" contains information that cannot be extracted from the particle flux. The spectrum of absorbed energy indicates the probability that a source particle and its subsequent radiation cascade will deposit a certain amount of energy in a detector.

The spectrum of absorbed energy for 10.0 MeV photons incident on a "detector" consisting of an 8.0 cm slab of aluminum is shown in Figure 12. The calculation was performed with the ITS Monte Carlo code. Note the peaks at 10.0, 9.489, and 8.978 MeV. Respectively, these correspond to radiation cascades in which all the energy of the incident photon is deposited in the detector, cascades in which the only energy not deposited is that associated with an escaping annihilation photon produced when a positron is absorbed, and cascades in which the only energy not deposited is that associated with two escaping annihilation photons. Deterministic codes can only calculate the energy that is deposited in the detector on the average over all possible particle cascades.

Another significant advantage of Monte Carlo codes is that the position, energy, and angle of each particle vary continuously. Since deterministic codes solve a transport equation by finite difference techniques, there is always some "discreteness" in their prediction. Such discreteness can affect the accuracy of deterministic calculations. Uncertainties due to discreteness are as fundamental to deterministic codes as statistical uncertainties are to Monte Carlo codes.

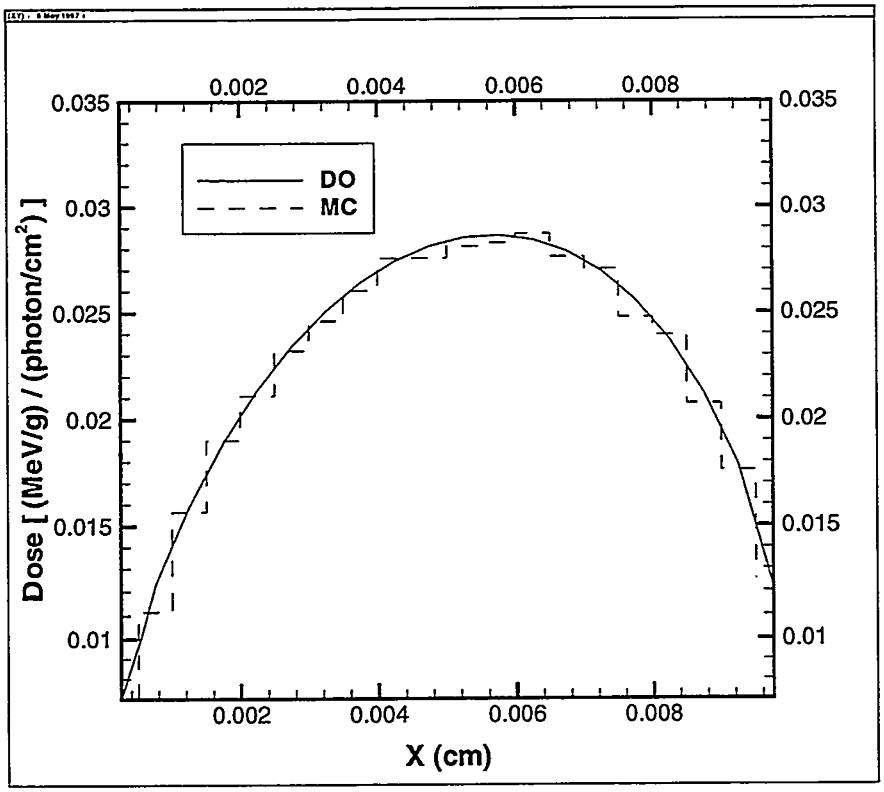

FIGURE 13. Dose-depth profiles for 1.0 MeV photons normally incident (from the left) on a 0.01-cm slab of gold.

Since coupled electron-photon Monte Carlo codes have been around a lot longer than similar deterministic codes, they presently have more advanced features. For instance, although robust 3D Monte Carlo codes exist, multidimensional deterministic codes for electron-photon transport are not generally available. The ITS code also permits electron transport to occur in external electromagnetic fields. Such capabilities have not yet been added to deterministic codes.

Monte Carlo codes have several inherent disadvantages relevant to deterministic codes. A significant disadvantage is that statistical error can make Monte Carlo codes computationally costly. Statistical uncertainty is least for integral quantities (e.g. dose in a large region, total number of escaping particles) and is greatest for differential quantities (e.g. dose in a small region.) Statistical error also makes Monte Carlo very inefficient for some types of problems (e.g. deep shielding calculations in which the radiation is substantially attenuated.)

Some types of output are also difficult for a Monte Carlo code to calculate. For instance, charge deposition inherently has more statistical error than energy deposition. This is because the deposition of charge is a localized phenomenon whereas energy deposition is not. For instance, for photon sources, charge is removed when an electron is created (at the start of the electron trajectory) and deposited when at electron is absorbed (at the end of the trajectory.) However, under multiple interaction theories, energy deposition occurs throughout the trajectory of the electron

Consider the case in which 1.0 MeV photons are normally incident on a slab of gold. The dose- and charge-deposition profiles calculated with Monte Carlo (MC) are shown in Figures 13 and 14 respectively, along with a comparison to a deterministic discrete ordinates (DO) solution.

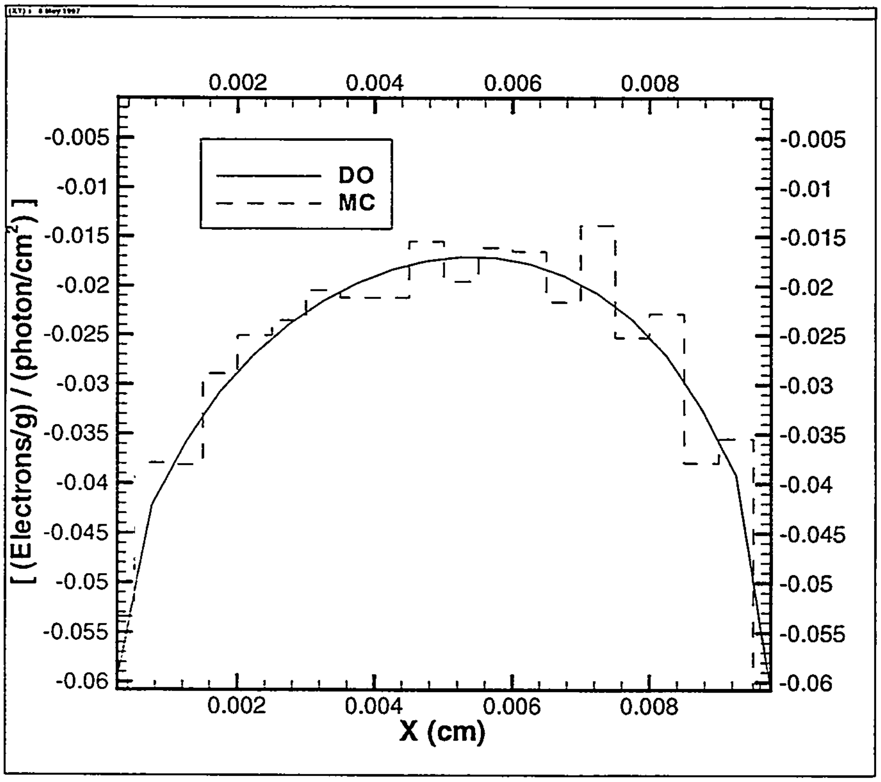

FIGURE 14. Charge-depth profiles for 1.0 MeV photons normally incident (from the left) on a 0.01-cm slab of gold

The "charge" deposition does not actually include the sign of the charge. A positive number indicates that a net number of electrons are deposited and a negative number indicates a net number of electrons are removed. The statistical error in the dose profile ranges from 2-4%. The error in the charge profile, produced in the same calculation with an identical number of photon source particles (one million), is 5-29%. This relatively large statistical error is responsible for the fluctuations in the charge profile.

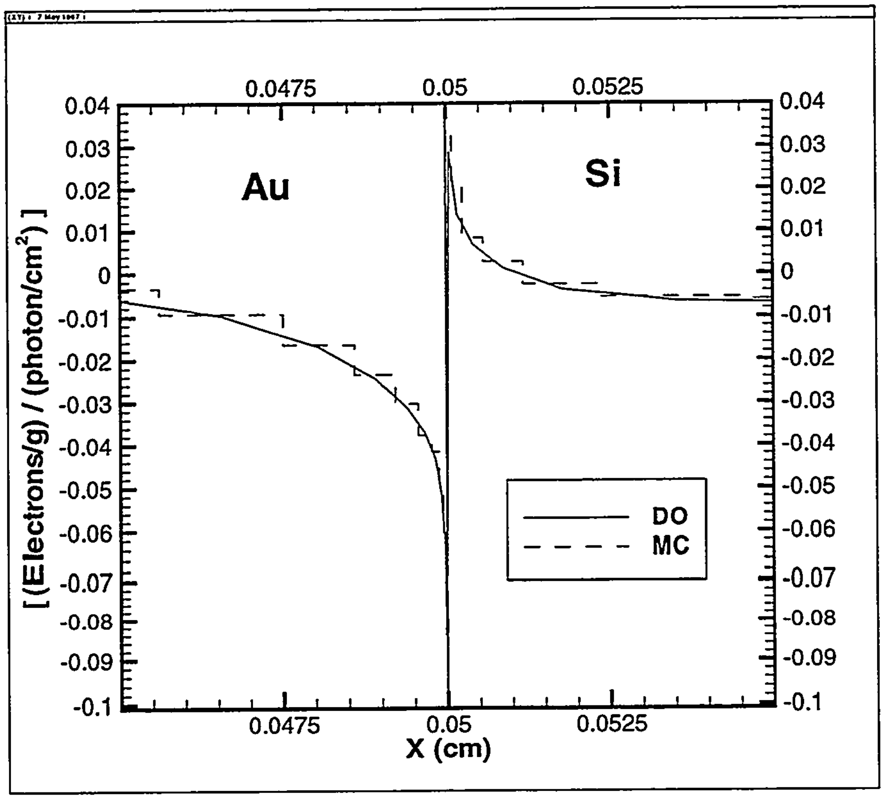

FIGURE 15. Charge-depth profiles at a material boundary for 1.0 MeV photons normally incident (from the left) on a 0.05-cm slab of gold followed by a 0.20-cm slab of silicon

Another feature of charge deposition profiles that make them difficult to calculate with Monte Carlo codes is that very high spatial resolution is often needed. Consider the case in which 1.0 MeV x-rays are normally incident on a slab of gold followed by a slab of silicon. The charge deposition profiles calculated with Monte Carlo (MC) are shown in Figure 15, along with a comparison to a deterministic discrete ordinates (DO) solution. Charge deposition determines the electromagnetic fields that can drive radiation response in electronics. As shown in the figure, most of this deposition occurs very close to the boundary.

The calculation of the charge distribution in thin layers with Monte Carlo codes is a very difficult task. The deterministic calculation took about two minutes on a workstation. The Monte Carlo calculation took 10^5 times as long. Since the analysis of radiation effects in electronics sometimes requires the calculation of the charge deposition profile, deterministic codes clearly have an advantage over Monte Carlo for this kind of prediction.

The prediction of radiation effects in electronics may also require the calculation of electron currents at material boundaries. These currents are generated by photoelectric and Compton processes. The response is determined by the difference between opposing electron currents. However, because of statistical error, calculation of this difference can also be a difficult task for Monte Carlo codes, especially in electronic configurations that have been "hardened" to be less susceptible to radiation

4.2 DETERMINISTIC

In deterministic methods, a finite-differenced form of a transport equation is solved [Duderstadt], [Lewis]. The discrete ordinates technique is the dominant deterministic method. It was refined at Los Alamos National Laboratory for neutral particle transport (neutrons and photons) in the early 1950s. The term discrete ordinates refers to generation of discrete angles.

The main advantage that deterministic methods have over Monte Carlo is speed. Precise solutions are possible for much less computational cost. Deterministic codes can be many orders of magnitude times faster than their Monte Carlo counterparts, depending on the output quantity of interest. However, deterministic codes typically require much more computer memory than Monte Carlo codes, especially for multi-dimensional calculations.

The main disadvantage of deterministic predictions is that they cannot represent the position, energy, and angle of the particle continuously. The accuracy of deterministic calculations is determined by the discrete representation employed. A deterministic solution will converge to the proper solution of the transport equation as the spatial domain is divided into more meshes, the energy domain is divided into more intervals or groups, and the angular domain is divided into more discrete directions. Published guidelines [Lorence (c)] can be used to estimate the number of meshes, groups, and/or directions needed for an accurate calculation.

A disadvantage of deterministic codes is that only information based on the particle flux can be obtained. This is because these codes explicitly solve a transport equation for the particle flux. However, the particle flux can be used to calculate many quantities of interest. For instance, dose is determined by folding the flux with an energy-deposition cross section (units of MeV/cm):

$$Dose\,(r) = \iint \sigma_E\,(r, E')\,\psi\,(r, E', \vec{\Omega}')\,dE'\,d\vec{\Omega}' \cdot \qquad \textbf{(13)}$$

For electrons, this cross section is essentially the stopping power. In coupled electron-photon transport, photons never deposit energy directly (except for a negligible amount due to photons that scatter below the cutoff energy.) Rather, dose is determined nearly entirely by the electron flux.

Similarly, charge deposition is obtained by folding the flux with an electron absorption cross section. Electron current can also be obtained from the flux. For instance, in a one-dimensional calculation, the escaping current of electrons at a boundary, r_B, is determined by:

$$Yield\,(r_B) = \iint (\vec{n} \times \vec{\Omega})\,\psi\,(r_B, E', \vec{\Omega}')\,dE'\,d\vec{\Omega}'. \qquad \textbf{(14)}$$

where the angular integral is over all outwardly-directed angles at the boundary whose surface normal is $\hat{n}$.

5.0 ELECTRON-PHOTON TRANSPORT CODES

5.1 MONTE CARLO

All modern production electron Monte Carlo codes are based on a seminal paper by Berger [Berger (b)]. The first ETRAN code, based directly on this work, was produced in 1968. Although its physical models are very sophisticated, ETRAN is restricted to simple geometries and is used primarily as a research tool. Developed independently, and perhaps even earlier, but employing many of the same concepts, was the BETA code [Jordan (a)]. This code and its derivatives, however, are multimaterial and multidimensional, and have been successfully applied to many complex engineering problems, especially in the aerospace industry.

In the 1970s, the electron physics of the ETRAN code was combined with a photon Monte Carlo code, detailed models of ionization and relaxation processes, and general three-dimensional modeling routines. The resulting code, SANDYL [Colbert], was the mainstay of weapon radiation effects research for many years and continues to be employed for this purpose.

However, the production code system from the ETRAN family that dominates today's applications is the ITS system. Basically, this system has extended the ETRAN model to multimaterial, multidimensional geometries, and has added new capabilities, such as the ionization/relaxation physics of the SANDYL code, macroscopic electric and magnetic fields, and geometry and trajectory plotting. Emphasis has been placed on user friendly input/output, efficiency, and robust operation, without sacrificing the rigor of the physical model. Recently, another code has joined the ETRAN family. The electron transport capability of ITS has been added to the neutral-particle MCNP code from Los Alamos National Laboratory.

The ETRAN code was originally developed for relatively low-energy problems (up to a few MeV.) Other codes were developed for very high-energy physics applications (up to 10^6 MeV) at about the same time. A six-year effort in the mid 70's resulted in the creation of a generalized code, EGS3 [Ford], for such applications. As the need arose for lower-energy applications, the EGS4 code [Nelson] was developed. This code enjoys wide use today, particularly in the medical physics community.

The EGS code uses a different form of condensed-history than the Class-1 scheme of the ETRAN family. In this approach, CSDA is used for soft inelastic collisions and hard collisions are modeled individually. This is the so-called Class-2 algorithm [Berger (b)]. Although EGS does not explicitly solve the Boltzmann-CSD transport equation, the separate treatment of soft and hard collisions is similar. The multiple-scattering treatment of elastic scattering in EGS is also different from that of ITS.

Adjoint Monte Carlo codes have also been developed. In adjoint transport, dose at a location can be calculated for many different sources in a single calculation. Adjoint Monte Carlo codes can also determine dose in a small volumes very efficiently. An adjoint option exists for the Monte

Carlo code, BETA. As part of the NOVICE code package [Jordan (a)], this feature has been applied for satellite shielding problems. Adjoint Monte Carlo options for electron transport have recently been added to existing general-purpose electron-photon Monte Carlo codes such as ITS [Lorence (b), Morel (a)] and MCNP.

5.2 DETERMINISTIC

Compared to Monte Carlo methods, deterministic techniques have only been recently applied to charged particle transport. In 1980, deterministic codes were developed to study ion transport in fusion reactors. A few years later, Morel developed a discrete ordinates method for electron transport [Morel (b-c)]. This approach was successfully implemented for coupled electron-photon transport and he adjoint transport capability demonstrated [Lorence (d)]. The discrete ordinates solution of the Spencer-Lewis equation has also investigated [Filippone (b)].

CEPXS/ONELD, the first general-purpose coupled electron-photon discrete ordinates transport code, was produced in 1989. This code was the product of a joint collaboration between Sandia National Laboratories and Los Alamos National Laboratory. The CEPXS/ONELD code effectively solves the Boltzmann-CSD equation in one-dimensional geometries. It uses a technique developed by Morel of "tricking" a Boltzmann transport code (which is most suitable for neutral-particle transport) to effectively the Boltzmann-CSD equation for the electron flux.

The CEPXS/ONELD code been used extensively for predicting radiation effects in electronics. It has been incorporated into the BOXIEMP II code for predicting internal electromagnetic pulse (IEMP) effects. [Walters].

Many new developments are underway in deterministic transport. A new version of the CEPXS/ONELD code called ADEPT is being developed at Sandia National Laboratories. This code will automatically select appropriate spatial mesh, energy intervals, and angular intervals for accurate discrete ordinates solutions. Work is also underway to develop 3D deterministic electron transport codes. These codes will use unstructured spatial meshes for maximum geometric flexibility and will be designed to operate on massively parallel computers.

6.0 PROTON TRANSPORT CODES

Monte Carlo techniques have been extensively employed for proton transport calculations. An example is LAHET [Prael], developed at Los Alamos National Laboratory. It evolved from the HETC code [Chandler] developed at Oak Ridge National Laboratory for the transport of nucleons, pions, and muons. LAHET is a Monte Carlo code with the same 3D geometry models of MCNP.

Secondary neutrons produced by protons can be important in satellite shielding calculations. For these calculations, the LAHET code can be used to predict the neutron flux, which can then be used as a source distribution for neutron transport calculation with MCNP.

7.0 ACKNOWLEDGMENT

Sandia is a multiprogram laboratory operated by Sandia Corporation, a Lockheed Martin Company, for the United States Department of Energy under Contract DE-ACO4-94AL85000.

8.0 REFERENCES

[AIC] AIC Software, P.O. Box 544, Grafton, MA 01519 (1994).

[Anderson] *The Stopping and Ranges of Ions in Matter, Vol. 3*, H.H. Anderson and J.F. Ziegler, Pergamon Press, (1977).

[Ashley] J. C. Ashley and V.E. Anderson, "Energy Losses and Mean Free Paths of Electrons in Silicon Dioxide," IEEE Trans. Nucl. Sci., 28 (6), 4132 (1981).

[Attix] *Introduction to Radiological Physics and Radiation Dosimetry*, F.H. Attix, John Wiley and Sons, 1986.

[Bell] *Nuclear Reactor Theory*, Y. I. Bell and S. Glasstone, Van Nostrand Reinhold Co., (1977).

[Biggs] F. Biggs and R. Lighthill, "Analytical Approximations for X-ray Cross Sections III", SAND87-0070, Sandia National Laboratories, (1988).

Berger (a)] M.J. Berger and S.M. Seltzer, "ETRAN Monte Carlo System for Electron and Photon Transport Through Extended Media," CCC-107, Oak Ridge National Laboratory, (1968)

[Berger (b)] M. J. Berger, Methods in Computational Physics, :Monte Carlo Calculation of the Penetration and Diffusion of Fast Charged Particles," Vol. 1, Academic, New York (1963).

[Briesmeister] J. F. Briesmeister, LA-12625-M, Los Alamos National Laboratory (1993).

[Brown] D. B. Brown, "The Phenomenon of Electron Rollout for Energy Deposition in MOS Devices," IEEE Trans. Nucl. Sci., 33 (6), 1240 (1986).

[Chandler] K.C. Chandler and T.W. Armstrong, ORNL-4744, Oak Ridge National Laboratory (1972).

[Chilton] *Principles of Radiation Shielding*, A.B. Chilton, J.K. Shultis, and R.E. Faw, Prentice-Hall, 1984.

[Colbert] H. M. Colbert, "SANDYL: A Computer Code for Calculating Combined Photon-Electron Transport in Complex Systems," Sandia National Laboratories Report SLL-74-0012, (1973).

[Davisson] C.M. Davisson and R.D. Evans, "Gamma-Ray Absorption Coefficients," Rev. of Mod. Phys., 24 (2), 79 (1952).

[Dellin] T.A. Dellin and C.J. MacCallum, IEEE Trans. Nucl. Sci., 23(6), 1844 (1976).

[Duderstadt] *Transport Theory*, J. J. Duderstadt and W. R. Martin, John Wiley and Sons, 1979.

[Filippone (a)] W.L. Filippone, "The Theory and Application of SMART Electron Scattering Matrices," Nucl.Sci. Eng., 99, 232 (1988).

[Filippone (b)]	W.L. Filippone and S.P. Monahan, "Path Length Differencing and Energy Conservation of the S_N Boltzmann/Spencer-Lewis Equation," Nucl. Sci. Eng., 113, 136 (1993).
[Ford]	R. L. Ford and W. R. Nelson, "The EGS Code System.: Computer Programs for the Monte Carlo Simulation of Electromagnetic Cascade Showers (Version 3)" Stanford Linear Accelerator Center Report, SLAC-210 (1978).
[Halbleib]	J. A. Halbleib, R. P Kensek, T. A. Mehlhorn, G. D. Valdez, S. M. Seltzer, M. J. Berger, "ITS Version 3.0: The Integrated TIGER Series of Coupled Electron / Photon Monte Carlo Transport Codes," SAND91-1634, Sandia National Laboratories, 1992.
[ICRU]	*Stopping Powers for Electrons and Positrons*, ICRU Report 37, 1984.
[Janni]	J.F. Janni, "Proton Range-Energy Tables, 1 keV - 10 GeV: Energy Loss, Range, Path Length, Time-of-Flight, Straggling, Multiple Scattering, and Nuclear Interaction Probability. Part 1, For 63 Compounds; Part 2, For Elements $1 \leq Z \leq 92$," Atomic Data and Nuclear Data 27, 147 (1982)
[Jenkins]	*Monte Carlo Transport of Electrons and Photons*, Eds. T. M. Jenkins, W. R. Nelson, and Alessandro Rindi, Plenum (1988).
Jordan (a)]	T. M. Jordan, "An Adjoint Charged Particle Transport Method" IEEE Trans. Nucl. Sci., 23, 1857 (1976).
[Jordan (b)]	T. M. Jordan, "Adjoint Electron Monte Carlo Calculations," Trans. Am. Nucl. Soc., 52, 382 (1986).
[Lamarsh]	J. R. Lamarsh, Introduction to Nuclear Reactor Theory," Addison-Wesley Publishing Company, 1972.
[Lewis]	*Computational Methods of Neutron Transport*, E.E. Lewis and W.F. Miller, Jr., John Wiley and Sons, Inc., 1984.
[Lockwood]	G.J. Lockwood, L.E. Ruggles, G.H. Miller, J.A. Halbleib, "Calorimetric Measurement of Electron Energy Deposition in Extended Media -- Theory vs. Experiment," SAND79-0414, Sandia National Laboratories, (1980).
[Lorence (a)]	L. J. Lorence, Jr., J. E. Morel, G. D. Valdez, "User's Guide to CEPXS/ONEDANT: A One-Dimensional Coupled Electron-Photon Discrete Ordinates Code Package, Version 1.0," SAND89-1661, Sandia National Laboratories, (1989).
[Lorence (b)]	L. J. Lorence, R.P. Kensek, J.A. Halbleib, J.E. Morel, "Adjoint Electron-Photon Transport Monte Carlo Calculations with ITS," IEEE Trans. Nucl. Sci., 42(6), 1895 (1995).
[Lorence (c)]	L. J. Lorence. Jr., J. E. Morel, G. D. Valdez, SAND89-2211, "Results Guide to CEPXS/ONELD:A One-Dimensional Coupled Electron-Photon Discrete Ordinates Code Package, Version 1.0," Sandia National Laboratories, (1990).
[Lorence (d)]	L.J. Lorence, Jr., W.E.Nelson, J.E. Morel, "Coupled Electron-Photon Transport Calculations Using the Method of Discrete Ordinates," IEEE Trans. Nucl. Sci., 32, 4416 (1985).
[Morel (a)]	J.E. Morel, L.J. Lorence, R.P. Kensek, J.A. Halbleib, D.P. Sloan, "Hybrid Multigroup Continuous-Energy Monte Carlo Method," Nucl. Sci. Eng., 124, 369 (1996).
[Morel (b)]	J.E. Morel, "Fokker-Planck Calculations Using Standard Discrete Ordinates Codes," Nucl. Sci. Eng., 79, 340 (1981).

[Morel (c)] J.E. Morel, " Multigroup Legendre Coefficients for the Diamond Difference Continuous Slowing Down Operator," Nucl. Sci Eng., 91, 324 (1985).

[Nelson] W. R. Nelson, H. Hirayama, and D. W. D. Rogers, "The EGS4 Code System." Stanford Linear Accelerator Center Report, SLAC-265 (1985).

[Perkins (a)] S.T. Perkins, D.E. Cullen, M.H. Chen, J.H. Hubbell, J. Rathkopf, and J. Scofield, UCRL-50400 Vol 30, Lawrence Livermore National Laboratory, (1991); D.E. Cullen, M.H. Chen, J.H. Hubbell, S.T. Prekins, E.F. Plechatcy, J.A. Rathkopf, and J. Scofield, "Tables and Graphs of Photon-Interaction Cross Sections from 10 eV to 100 GeV Derived from the LLNL Evaluated Photon Data Library (EPDL)," UCRL-50400 Vol 6 (Parts A and B), Lawrence Livermore National Laboratory, (1991).

[Perkins (b)] S.T. Perkins, D.E. Cullen, S.M. Seltzer, "Tables and Graphs of Electron-Interaction Cross Sections from 10 eV to 100 GeV Derived from the LLNL Evaluated Electron Data Library (EEDL)," UCRL-50400 Vol 31, Lawrence Livermore National Laboratory, (1991)

[Prael] R.E. Prael and H. Lichtenstein, LA-UR-89-3014, Los Alamos National Laboratory (1989).

[Przybylski] K. Przybylski and J. Ligou, "Numerical Analysis of the Boltzmann Equation Including Fokker-Planck Terms," Nucl. Sci. Eng., 81, 92 (1982).

[Seltzer] S. Seltzer, "SHIELDOSE: A Computer Code for Space-Shielding Radiation Dose Calculations," NBS Technical Note 1116, National Bureau of Standards (1980).

[Turner] C. D. Turner, "The Sandia Total-Dose Estimator: SANDOSE Description and User Guide," SAND94-3130, Sandia National Laboratories (1995).

[Woolf] S. Woolf and J.N. Bradford, "Monte Carlo Simulation and Analysis of Elastic and Inelastic Scattering of Electrons in Insulators," IEEE Trans. Nucl. Sci., 34 (6), 1392 (1987).

[Zerby] C.D. Zerby and F.L. Keller, "Electron Transport Theory, Calculations, and Experiments," Nucl. Sci. and Eng., 27, 190 (1967).

[Walters] D. Walters, J. Wondra, W. Seidler, L.J. Lorence, J. E. Morel, W. Walters, F. Brinkley, G.D. Valdez, "User's Handbook for BOXIEMP II: A Gamma Ray Transport, Photocompton Emission and IEMP Coupling Code," J205-92-0195/2703, Jaycor (1992).

II. RADIATION TRANSPORT PHENOMENA AND MODELING

PART B: APPLICATIONS WITH EXAMPLES

David E. Beutler
Sandia National Laboratories
P. O. Box 5800, Mail Stop 1179
Albuquerque, NM 87185-1179

1.0 Introduction

In the previous sections Len Lorence has described the need, theory, and types of radiation codes that can be applied to model the results of radiation effects tests or working environments for electronics. For the rest of this segment, we will concentrate on the specific ways the codes can be used to predict device response or analyze radiation test results. Regardless of whether one is predicting responses in a working or test environment, the procedures are virtually the same. The same can be said for the use of 1-, 2-, or 3-dimensional codes and Monte Carlo or discrete ordinates codes. No attempt is made to instruct the student on the specifics of the code. For example, we will not discuss the details, such as the number of meshes, energy groups, etc. that are appropriate for a discrete ordinates code. For the sake of simplicity, we will restrict ourselves to the 1-dimensional code CEPXS/ONELD [1]. This code along with a wide variety of other radiation codes can be obtained from the Radiation Safety Information Computational Center (RSICC) [2] for a nominal handling fee. This center severs as an archive and distribution point for radiation transport codes and information.

Indeed, it is usually wise to design an experiment that can easily be approximated in 1-dimension, if at all possible. The level of complication, required experimental details, and computer resources grows dramatically for multi-dimensional problems. Although, in principle, it might seem better to mock up the actual radiation environment and geometry as closely as possible in an experiment. This may not be practically viable. If the test environment and geometry are still different enough to require analysis, then this tact will require significant resources just for the design and analysis of the experiment alone to produce usable results.

As discussed earlier, the algorithmic convergence of the CEPXS/ONELD code is roughly 5%. Therefore, we assume in our discussions here that disagreements between different predictions less than or equal to 5% are not significant. In addition, I cannot overemphasize the importance of looking at the diagnostic output of these codes. Monte Carlo codes usually give an estimate of the statistical uncertainty of each calculated quantity. If the uncertainty is > 10%, the value in question is suspect and more histories should be run. For discrete ordinates codes, usually the quality of charge and energy conservation is reported. Regardless of whether a converged solution was obtained, if any of these values is < 99%, the solution is suspect, and the problem should be run using a finer energy/spatial mesh.

All the codes mentioned previously are time independent codes; that is, they assume the material properties, spectrum, fluence, external electric and magnetic fields are all constant in time. When this is not the case, the codes can be used to solve a problem at each point in time of the irradiation with different input conditions in an iterative scheme. Examples of this are time dependent spectrometers [3] and spacecraft charging of dielectrics [4], where the internal electric fields change as a function of dose. Another limitation of the codes is that they do not predict **measured** responses in electronics or even many types of dosimeters. These codes have been carefully benchmarked [5], do an outstanding job of radiation transport, and can be used to predict energy and charge deposition, spectra, and fluence, but that is where they stop. Additional codes and/or models are necessary to predict the resulting trapped charge in an oxide or photocurrent in a junction. For example, if the radiation transport code predicts the dose in a p-n junction, this needs to be converted to a number of electron-hole pairs, and transported through the circuit. This can often be done using codes such a PSPICE[6] or DAVINCI [7] to obtain the prediction for the response. For our discussions we will restrict ourselves to the results obtained from the radiation transport calculation alone.

In the remaining sections we will analyze two irradiation experiments, one using photons and the other electrons, and one working environment, proton irradiation in a space environment. Because the specific input file is code dependent, we will not go into great detail on keywords or options. Instead, we will concentrate on the different problems the codes can be used to solve, the information the user must be prepared to provide, and the interpretation of the output. One important use of these codes that will be emphasized is experiment design. Using careful design and analysis before fielding an experiment, many problems and ambiguities usually discovered after the test can be avoided.

2.0 X-Ray or γ–Ray Irradiation

One of the first tasks in designing an experiment is the selection of the irradiation facility or facilities. Along with dose-rate and coverage area, an important aspect of the selection process is the spectrum and how it compares with the working environment. Differences in spectra can lead to differences in response that need to be addressed. This can be as simple as accounting for differences in attenuation or dose-enhancement from the package or very complex as in the case of different gate metallizations. If ICs with different fabrication materials are irradiated at the same time or if there are different materials on some contacts than others on the same IC, it may not be possible to unambiguously correlate the test environment to the working environment. The calculations discussed below can be used to address these issues and should be done in advance of the experiment.

We will discuss two experimental setups: One using a ^{60}Co spectrum and the other a bremsstrahlung spectrum. The experimental setups are shown in Figures 1 and 2 respectively. For the ^{60}Co setup the device under test (DUT) is placed in a box made of 0.7-mm-thick aluminum surrounded by 1.5-mm of lead as specified by ASTM standard E 1249 [8]. For the flash x-ray (FXR) facility electrons are accelerated into a high-Z (atomic number) target producing bremsstrahlung. These x rays impinge on a test fixture on the right containing the DUT. The test fixture is a Faraday cage to prevent RF and EMP noise generated by the accelerator from entering the fixture. The lead collimator and rear shield reduce the radiation exposure on the rest of the test circuitry and cables. These geometries are typical of many x-ray tests and the reasons for some of the features are discussed below.

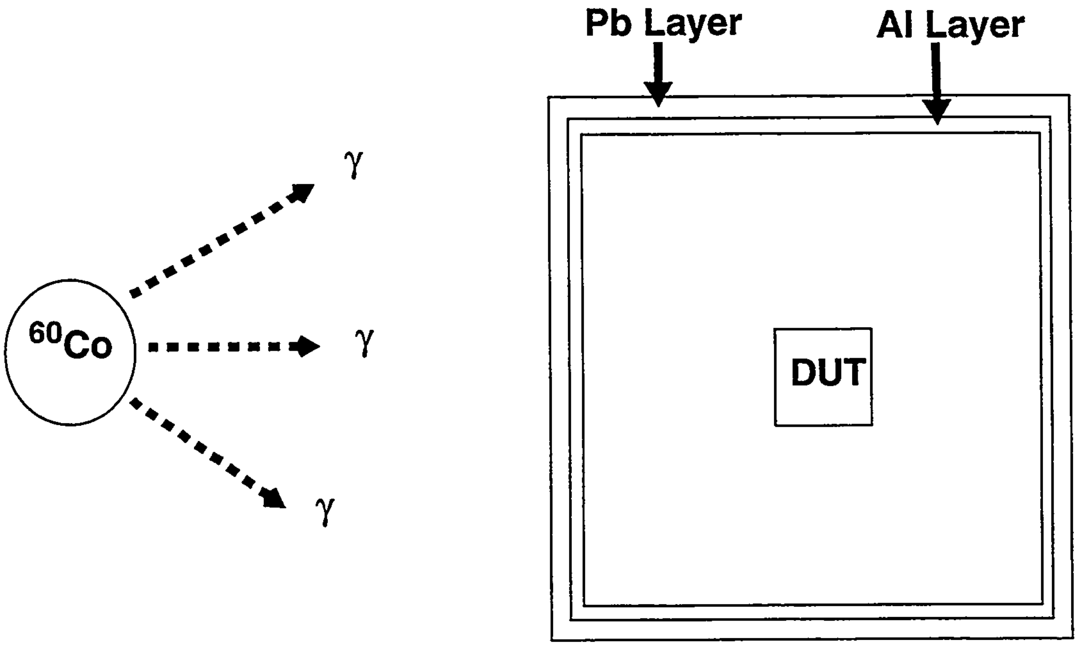

Figure 1: Schematic of ^{60}Co irradiation with DUT surrounded by the standard lead/aluminum box.

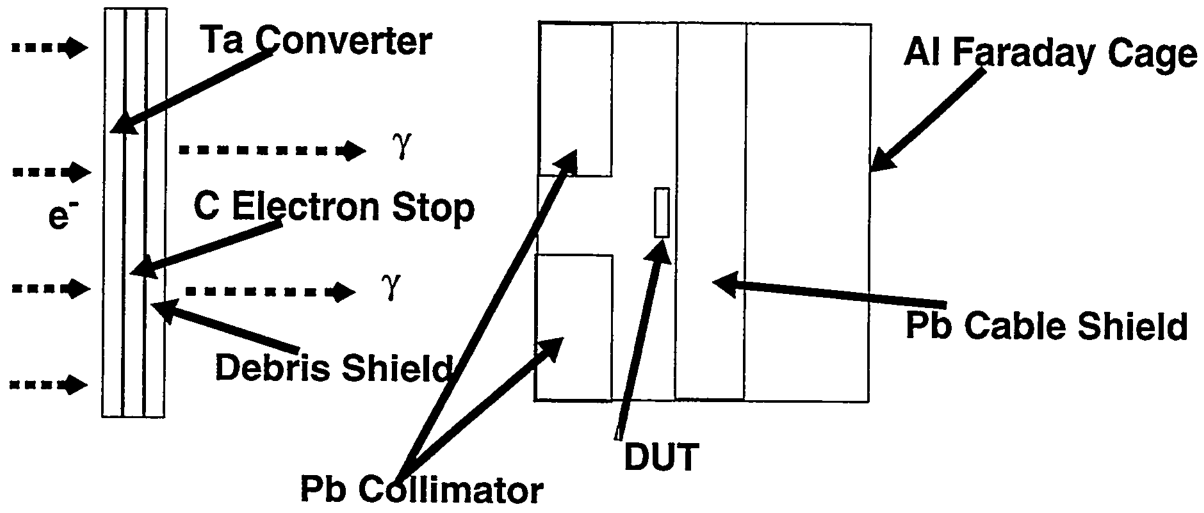

Figure 2: Schematic of FXR irradiation with electrons impinging on bremsstrahlung converter on the left and the DUT in a Faraday cage with lead collimation and shielding.

2.1 Photon Spectrum Calculation

Unfortunately, the spectrum at most irradiation facilities is not well known. It is very rare to have a measured spectrum in a ^{60}Co cell. This is not because we do not know the decay products of ^{60}Co. It is because this spectrum is significantly altered by the source/cell scatter and attenuation. This altered spectrum can be very difficult to measure, especially in a small cell. The calculation requires a detailed model of the cell geometry and materials and a 3-dimensional radiation transport code. In addition, changes to the room geometry and materials require a new measurement or calculation.

The ASTM E 1249 [8] test standard alleviates many of these problems with the use of a lead/aluminum box. This minimizes (but does not eliminate) the variations in device response from cell to cell by attenuating a large fraction of the scattered fluence of low-energy photons. In Figure 3 we plot a calculated ^{60}Co spectrum using the "Collimator" code [9] from a typical large room source [10], and the transmitted spectra through the lead/aluminum box. The box clearly attenuates photons below 400 keV but not completely until ~180 keV. In addition, the box emits lead K lines (~80 keV) into the interior. Although this calculation demonstrates the radiation transport capability and the potential problems encountered. ^{60}Co spectra vary from source to source. The ASTM E 1249 [8] test standard gives a number of spectra for different types of facilities and should be consulted to estimate responses for a specific facility.

At these lower energies the concept of dose-enhancement becomes important. Dose is the energy per unit mass absorbed in the material that is imparted by the radiation. Kerma (kinetic energy released per unit mass) is the energy released in the material, primarily in the form of secondary electrons. If all the energy released is absorbed then the kerma would be equal to the dose. Unfortunately this is often not the case for two reasons. First, when the energy of the secondary electrons is above 1 MeV, the production of bremsstrahlung is significant. The photons produced in this process are rarely absorbed in the geometry of interest and the energy is lost. If this energy loss, due to bremsstrahlung yield, is subtracted from the kerma, we obtain the equilibrium dose. Equilibrium dose occurs when there is no net flow of charged particles in or out of the region of interest (charged particle equilibrium) and is typically the dose measured by a dosimeter by design. Second, in electronic devices, charged particle equilibrium is often not present. This is due to the material dependence of the production of secondary electrons from the photoelectric effect, and the transport of these electrons from one thin layer to another. The dose-enhancement factor is defined to be the ratio of the absorbed dose to the equilibrium dose in the material of interest. Ideally this number should be 1. Then the calculation of dose in the device can be easily correlated to the dose in a dosimeter measuring an equilibrium dose. The calculation of dose enhancement has been a topic of interest for many years and a few representative papers are listed in Reference 11.

The dose-enhancement sensitivity of a 100-nm gate oxide in a standard gold/Kovar lidded ceramic packaged device is shown in Figure 4. The shape of this curve is typical of this effect when interfaces of different materials are involved. The dose-enhancement is greatest near 100 keV where the electron ranges are long compared to the thicknesses of the device layers and the photoelectric effect is dominant. At higher energies incoherent scattering dominates and does not produce dose-enhancement, because it is relatively insensitive to material. At lower energies the range of the secondary electrons emitted from the gold is too small to deposit dose in the oxide. Figures 3 and 4 demonstrate that although this box eliminates most of the photon spectrum that contributes to dose enhancement, it does not remove all of it and dose-enhancement factors greater than 10 are possible. Therefore, variations in the spectrum below ~400 keV from facility to facility may cause variations in the device response. Possible improvements to this box will be discussed later in the shielding section.

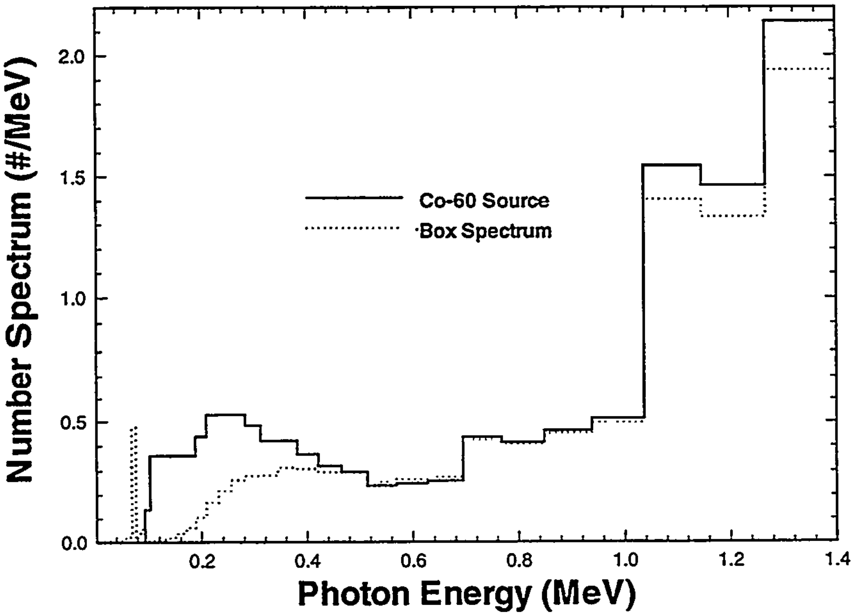

Figure 3: Plot of photon number spectrum as a function of energy for a large ^{60}Co room source and the resulting spectrum after transport through the lead/aluminum box.

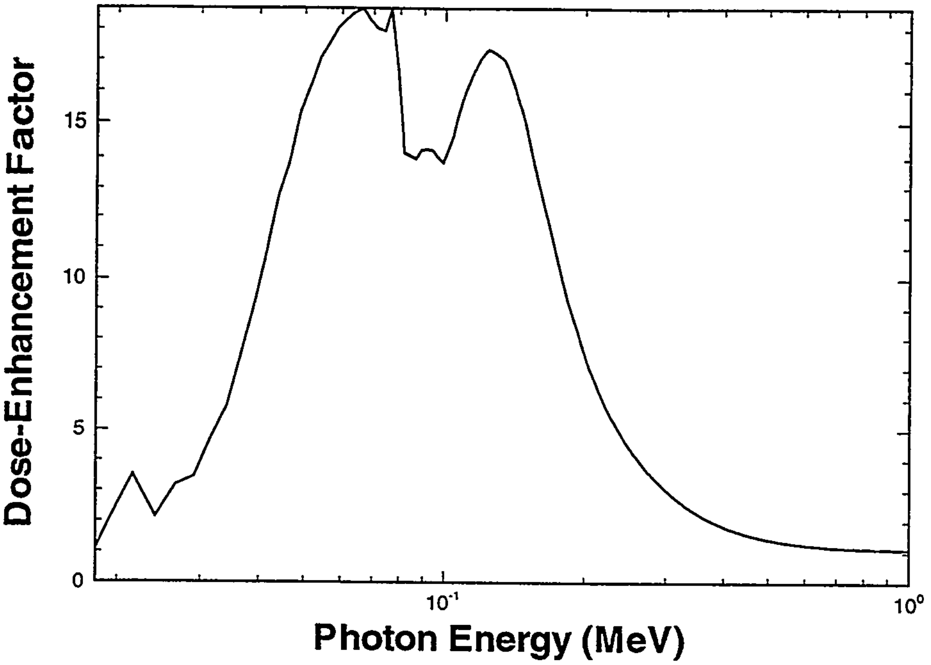

Figure 4: Plot of the dose enhancement factor as a function of energy for a a standard gold/Kovar lidded ceramic packaged device. (An absence of dose enhancement has a value of 1.)

The calculation of the spectrum inside the box (Figure 3) required the input photon spectrum (often hard to obtain) and the thicknesses of the lead/aluminum box. (The additional input of density is not required for pure elements at STP.) The units used in CEPXS/ONELD and ITS are MeV, g, and cm for energy, mass, and length. The annotated copy output of the CEPXS/ONELD code for this calculation is shown in Table 1.

The input requires the spectrum be expressed as a normalized integral number spectrum (number of photons vs. energy (MeV)), that is, the fraction of photons with energies below a particular energy. (See Table 1 for an example.) If your input spectrum is not in this form it must be converted. Number spectra are used because of their ease of use in Monte Carlo calculations, where individual photons and electrons are counted. A differential energy spectrum (energy/energy vs. energy) can be converted to a differential number spectrum (number of photons/energy versus energy) by dividing the energy in **each** bin by the average energy of the bin.

$$(\#/\text{MeV}) = (\text{MeV}/\text{MeV})/(<\text{energy (MeV)}>_{\text{bin}}). \tag{1}$$

Table 1: Output of Transport Calculation of ^{60}Co Through Lead/Aluminum Box

```
********************************************************************************   ADEPT version of CEPXS/ONELD
*                                             *                                    Automatic Discretization Electron-
*        INPUT TO ADEPT  (MAR 13, 1992)                                      *     Photon Transport
*                                             *
********************************************************************************

                                                                                   copy of input deck
title 1                                                                            number of lines in title
fredrickson degraded cobalt 60 spectrum into astm box                              title
cutoff 0.001                                                                       minimum energy used 0.001 MeV
photon-source                                                                      photon source
material Pb                                                                        materials listed by standard abbreviations
material Al                                                                        standard densities assumed for elements
layers 2                                                                           number of layers
1 0.15                                                                             material index and thickness in cm
2 0.07
spectrum 14                                                                        number of bins in spectrum
1.0 0.72 0.703 0.397 0.353 0.297 0.258 0.213 0.187 0.163 0.131 0.089 0.036 0       fraction of photons below an energy
energies                                                                           the energy bins for the spectrum
1.4 1.3 1.2 1.1 1.0 0.9 0.8 0.7 0.6 0.5 0.4 0.3 0.2 0.1
output                                                                             output options follow
currp                                                                              photon currents requested
```

Table 1: Output of Transport Calculation of ^{60}Co Through Lead/Aluminum Box Continued

```
***********************************************************************        Output
*                                                 *
*           PROBLEM DEFINITION                          *
*                                                 *
***********************************************************************

                                                                               list of materials and densities used
  LAYER      THICKNESS     MATERIAL       DENSITY

    1        1.5000E-01       1        1.1400E+01
    2        7.0000E-02       2        2.7000E+00

Plane-Wave at Angle of Incidence =  8.3494E+00 Degrees                         average angle of normal incidence bin
Default Electron Groups =  58                                                  number of electron groups
Default Photon Groups =  58                                                    number of photon groups
Default SN Order = 16                                                          number of angle groups
Default Number of Spatial Meshes =   13                                        number of spatial groups


1***********************************************************************
*                                                 *
*               OUTPUT (IBM)                             *                     AIX IBM version
*                                                 *
*          AVERAGE SOURCE ENERGY =  9.9530E-01 MeV            *                average energy of source
*                                                 *                            This number is useful for converting to
*        ALL QUANTITIES NORMALIZED TO A SINGLE SOURCE PARTICLE    *            numbers normalized to energy fluence.
*                                                 *
*     FOR A SLAB, THIS IS THE SAME AS NORMALIZING TO A           *
*     UNIT NUMBER FLUX (SOURCE PARTICLES/CM2)                  *
*                                                 *                            Not important at low energies and was
*     NO PAIR SECONDARIES PRODUCED                        *                    disabled. Energy is deposited but particles
*                                                 *                            not transported.
*   SPATIAL MESH AND GROUP STRUCTURE OPTIMIZED FOR    DOSE        *            OK, because electron currents not
*                                                 *                            selected.
***********************************************************************
```

Table 1: Output of Transport Calculation of ^{60}Co Through Lead/Aluminum Box Continued

```
REVERSE PHOTON YIELD AT START OF LAYER

    LAYER      NUMBER/SOURCE

     1       2.0181E-02
     2       3.3146E-03
```

reverse emission of photons at start of each layer

```
FORWARD PHOTON YIELD AT END OF LAYER

    LAYER      NUMBER/SOURCE

     1       8.7019E-01
     2       8.6693E-01
```

forward emission of photons at end of each layer

Note that ~87% of photons transport through box. (Yield at end of layer 2.)

```
NET FORWARD PHOTON YIELD AT START OF LAYER

    LAYER      NUMBER/SOURCE

     1       9.7982E-01
     2       8.6688E-01
```

forward of previous layer minus reverse of layer

```
REVERSE CHARGED-PARTICLE YIELD AT START OF LAYER

    LAYER      NUMBER/SOURCE

     1       3.2288E-03
     2       1.6397E-03
```

same for information for electrons

Note that very few electrons are emitted.

```
FORWARD CHARGED-PARTICLE YIELD AT END OF LAYER

    LAYER      NUMBER/SOURCE

     1       5.8767E-03
     2       5.1300E-03
```

Table 1: Output of Transport Calculation of ^{60}Co Through Lead/Aluminum Box Continued

```
NET FORWARD CHARGED-PARTICLE YIELD AT START OF LAYER

   LAYER      NUMBER/SOURCE

     1      -3.2288E-03
     2       4.2370E-03


TOTAL PHOTONS        ENERGY FORWARD ESCAPE =  9.0077E-01 MeV/Source
TOTAL PHOTONS        ENERGY REVERSE ESCAPE =  3.5242E-03 MeV/Source
TOTAL CHRGD-PARTICLES ENERGY FORWARD ESCAPE =  2.7912E-03 MeV/Source
TOTAL CHRGD-PARTICLES ENERGY REVERSE ESCAPE =  9.7207E-04 MeV/Source
```

photon energy transmitted, 90% of source
photon energy reflected
electron energy transmitted, very small
electron energy reflected, very small

```
**************************************************************************

  LAYER    MASS-THICKNESS     DOSE DEPOSITION
             (g/cm2)           (MeV-cm2/g)

    1       1.7100E+00        4.6857E-02
    2       1.8900E-01       2.2898E-02

TOTAL ENERGY DEPOSITED =  8.4454E-02 MeV/source

**************************************************************************
```

mass thickness is the same as areal density

dose deposited in each layer, can be easily converted to Gy or rad

energy of source deposited in materials 9% of source energy

```
RESIDENT KERMA (DERIVED FROM PHOTON-FIELD ONLY)

  LAYER     MATERIAL    DOSE (MeV-cm2/g)

    1        1          4.9070E-02
    2        2          2.4519E-02

**************************************************************************
```

This is the equilibrium dose that would have been deposited in the layer from the photon fluence. Note that it is assumed that none of the bremsstrahlung from secondary electrons is absorbed in the layer in which it is created. Therefore, it is subtracted from the kerma, so that this quantity is equal to the equilibrium dose, especially at high energies where bremsstrahlung is significant.

Table 1: Output of Transport Calculation of ^{60}Co Through Lead/Aluminum Box Continued

```
 LAYER    MASS-THICKNESS    CHARGED-PARTICLE DEPOSITION
            (g/cm2)           (Particles-cm2/g)

   1       1.7100E+00        -4.3660E-03
   2       1.8900E-01        -4.7249E-03

TOTAL CHARGED PARTICLES =  -8.3588E-03 per source
```

Charged particle deposition
units are electrons per mass density
negative numbers mean that electrons are emitted from this layer
positive numbers mean electrons are deposited in this layer
only 0.008 electrons emitted per photon
not much charging

```
***************************************************************************


ENERGY CONSERVATION RATIO =   9.9720E-01
```

should be very close to 1, if not, results are suspect

```
 LAYER    CHARGED-PARTICLE CONSERVATION RATIO

   1       1.0000E+00
   2       9.9999E-01
```

should be very close to 1, if not, results are suspect

```
***************************************************************************


FORWARD PHOTONS        ENERGY SPECTRUM AT X =   2.2000E-01 cm

 energy (MeV)     number/MeV      number

 1.4000E+00      1.9385E+00
 1.2667E+00      1.9385E+00     2.5847E-01
 1.2667E+00      1.3311E+00
 1.1460E+00      1.3311E+00     1.6058E-01
 1.1460E+00      1.4049E+00
 1.0369E+00      1.4049E+00     1.5334E-01
 1.0369E+00      4.9706E-01
```

photons emitted from aluminum

Output is formatted to easily be plotted as a histogram, where x is energy and y is number/MeV.
Note that this is a differential number spectrum.
Number is the number/MeV multiplied by the bin width. Hence this is the number in the energy bin

Table 1: Output of Transport Calculation of ^{60}Co Through Lead/Aluminum Box Continued

```
 9.3813E-01   4.9706E-01   4.9085E-02
 9.3813E-01   4.4985E-01
 8.4879E-01   4.4985E-01   4.0192E-02
 8.4879E-01   4.0592E-01
 7.6795E-01   4.0592E-01   3.2813E-02
 7.6795E-01   4.2325E-01
~~~~~~~~~~~~~~~~~~~~~~~~~~~~~~~~~~~~~~~~~~
~~~~~~~~~~~~~~~~~~~~~~~~~~~~~~~~~~~~~~~~~~
output abbreviated
~~~~~~~~~~~~~~~~~~~~~~~~~~~~~~~~~~~~~~~~~~
~~~~~~~~~~~~~~~~~~~~~~~~~~~~~~~~~~~~~~~~~~
 5.4126E-03   5.1771E-04   5.1528E-07
 5.4126E-03   3.7056E-04
 4.4173E-03   3.7056E-04   3.6882E-07
 4.4173E-03   2.4807E-04
 3.4220E-03   2.4807E-04   2.4690E-07
 3.4220E-03   1.5171E-04
 2.4267E-03   1.5171E-04   1.5100E-07
 2.4267E-03   1.5929E-03
 1.0000E-03   1.5929E-03   2.2727E-06
```

These results assume 1 source particle per cm^2

```
TOTAL FORWARD PHOTONS      PER SOURCE =  8.6693E-01 AT X =  2.2000E-01

DIFFERENTIAL DOSE PROFILE

    x (cm)         dose(MeV-cm2/g)   Mesh(g/cm2)  Material  Layer

  6.38582330E-03    4.045881E-02     1.455968E-01    1      1
  1.96859082E-02    5.345736E-02     1.576452E-01    1      1
  3.35144315E-02    5.266354E-02     1.576452E-01    1      1
  4.73429548E-02    5.117379E-02     1.576452E-01    1      1
  6.11714780E-02    4.979058E-02     1.576452E-01    1      1
  7.50000013E-02    4.855948E-02     1.576452E-01    1      1
  8.88285246E-02    4.742372E-02     1.576452E-01    1      1
  1.02657048E-01    4.634096E-02     1.576452E-01    1      1
```

fraction of photons emitted from aluminum, 87%

dose in each spatial element

material and layer index are identified for each spatial element or subzone

These data are good for obtaining depth-dose profiles.

Table 1: Output of Transport Calculation of ^{60}Co Through Lead/Aluminum Box Continued

```
1.16485571E-01    4.524448E-02    1.576452E-01   1   1
1.30314094E-01    4.401611E-02    1.576452E-01   1   1
1.43614179E-01    3.489985E-02    1.455968E-01   1   1
1.80078711E-01    2.363912E-02    1.624250E-01   2   2
2.15078712E-01    1.836701E-02    2.657498E-02   2   2


RESIDENT DIFFERENTIAL KERMA PROFILE
 DOSE DERIVED FROM PHOTON-FIELD ONLY

   x (cm)        dose (MeV-cm2/g)   Mesh(g/cm2)  Material  Layer

6.38582330E-03    5.527127E-02    1.455968E-01   1   1
1.96859082E-02    5.458145E-02    1.576452E-01   1   1
3.35144315E-02    5.295571E-02    1.576452E-01   1   1
4.73429548E-02    5.141869E-02    1.576452E-01   1   1
6.11714780E-02    5.004419E-02    1.576452E-01   1   1
7.50000013E-02    4.880944E-02    1.576452E-01   1   1
8.88285246E-02    4.767148E-02    1.576452E-01   1   1
1.02657048E-01    4.658388E-02    1.576452E-01   1   1
1.16485571E-01    4.548950E-02    1.576452E-01   1   1
1.30314094E-01    4.429428E-02    1.576452E-01   1   1
1.43614179E-01    4.263393E-02    1.455968E-01   1   1
1.80078711E-01    2.453163E-02    1.624250E-01   2   2
2.15078712E-01    2.443920E-02    2.657498E-02   2   2
```

equilibrium dose in each spatial element material and layer index are identified for each spatial element or subzone

When compared to the dose profile, this can be used to indicate the amount of dose enhancement in a material. Because dose enhancement takes place near the interface, it often is not observable for thick layers unless the profile is examined and has an adequate number of zones in the layer. For example, two zones in the thick aluminum are not sufficient.

A differential number spectrum can be converted to a normalized integral number spectrum summing the number of photons below the upper energy edge of each bin. This can be expressed as:

$$INF_E = \left(\sum_{E = E_{min}}^{E} \gamma \bullet \Delta E_{bin} \right) \Big/ \left(\sum_{E = E_{min}}^{E_{max}} \gamma \bullet \Delta E_{bin} \right), \qquad (2)$$

where INF_E is the integral number fraction at a particular energy, E_{min} is the minimum energy, E_{max} is the maximum energy, γ is the number of photons per unit energy in the bin, and ΔE_{bin} is the width of the energy bin. This sounds complicated, but can be easily be accomplished in a spread sheet.

Take care to convert energy units of calories or keV to MeV where appropriate. The spectrum is normalized by dividing by the total number of photons. Hence the input spectrum always has a fluence of 1 photon/cm^2 or 1 photon for a pencil beam case, where the target is much larger than the source. The input energy fluence is the 1 photon/cm^2 times the average energy of the input spectrum. Fortunately, CEPXS/ONELD calculates and prints the average energy of the input spectrum near the beginning of the output (Table 1).

The forward 2π leakage or output spectrum is a differential number spectrum. It can converted to a differential energy spectrum by multiplying the number of photons in each bin by the average energy of the bin (the inverse of Eq. 1). In addition, if you want to use the differential number spectrum as input for another calculation, you must convert it to a normalized integral number spectrum (Eq. 2).

For the case of a flash x-ray machine, the facility may provide you with a spectrum. If not, or you may want to check it anyway, you can calculate the bremsstrahlung spectrum using the current and voltage waveforms from the accelerator located near the anode-cathode gap. Using the appropriate time-aligned, frequency-compensated, and inductance-corrected waveforms, an electron spectrum (number of electrons/energy versus energy) can be calculated. This can be converted in the same fashion as above to a normalized integral number spectrum with a fluence of 1 electron/cm^2. Then, using the electron spectrum, the angle of incidence of the electrons on the target, and the thicknesses and densities of the target materials, the output spectrum can be calculated. (Many FXR designers use these codes to calculate the optimum target geometry [12].) Because the bremsstrahlung spectrum is a function of angle off normal from the converter, you may want to calculate the spectrum for a specific angular bin. (Remember, Monte Carlo and discrete ordinates codes bin their outputs in angle, energy, and space.) For example, if the IC is up close to the accelerator, the forward 2π spectrum is probably appropriate, because photons over a wide range of angles are used. If the fixture is backed off from the convertor then the 0 degree angular bin is probably appropriate, because the x rays are normally incident. Because a typical CEPXS/ONELD calculation uses 16 angular groups the 0° bin actually encompasses angles from $0^{\circ}$to 13°. A comparison of the 0°-13° and forward 2π calculated spectra for the Sandia Sphinx facility is shown in Figure 5. Note that the spectrum is a little softer normal to the converter. This is because at these energies (2.6-MeV electron beam energy) the lower energy photons are attenuated more by the converter at large angles. The opposite is true for higher energy bremsstrahlung, where the spectrum is softer at large angles due to scattering in the converter.

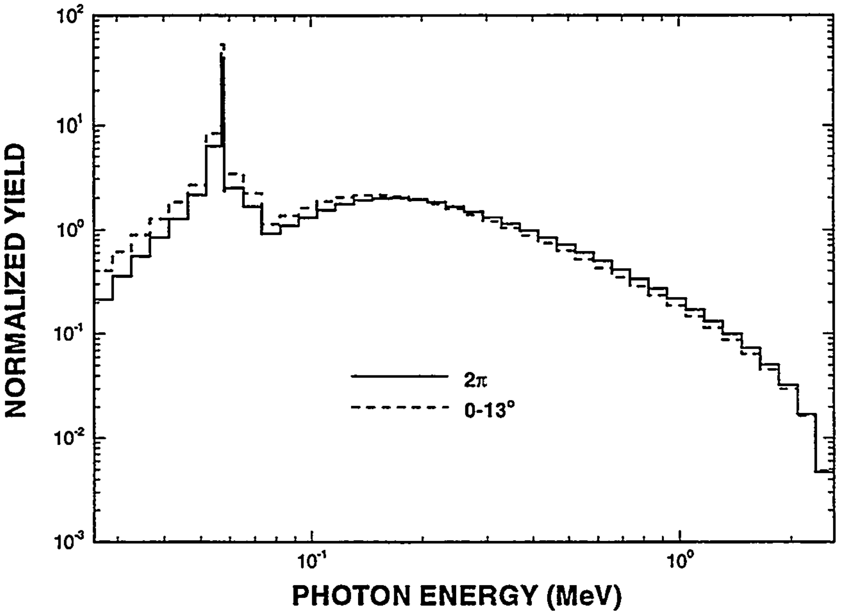

Figure 5: Plot of calculated normalized bremsstrahlung differential number spectra as a function of energy from SPHINX for the 0^{O}-130^{O} angular bin and the forward 2π.

At this point you have a calculated spectrum. The question is: How accurate is it? Compare your spectrum to the facility spectrum and hopefully a measured spectrum. For DC x-ray sources one can use germanium pulse-height detectors with a multi-channel analyzer to produce a pulse-height distribution that approximates the spectrum. Using ITS, you can calculate the pulse-height distribution using your calculated spectrum as a check [13]. (Remember, only Monte Carlo codes can calculate correlated quantities, such as pulse-height distributions.) However, this technique is impractical for FXRs and spectral unfolds using arrays of filtered dosimeters are common [14]. A comparison to the spectral unfold will give you a good idea of the quality of your spectrum. If they don't agree, you will have to decide which to use.

If the measured and calculated spectra don't agree, you can check the spectrum using ASTM standard E 665 [15]. This measures the depth-dose profile using dosimeters and different thickness absorbers. Calculate the dose (see Section 2.3 on calculating dose in the dosimeter) in the dosimeters using all available spectra and compare with your measurements. If they agree than your spectrum is close to being correct. If, not it's time to consult the facility. You may have to guess a spectrum and check it through trial and error using the codes. Fortunately, most of the time this will not be necessary.

In many cases the FXR spectrum may be different than the working environment for the device. In addition to dose-enhancement, which will be discussed below, one should consider differences in the deposition profile. The important feature here is that, if the spectrum is radically different than the working environment, the variation in dose as a function of position in a device may change. As an example, high Z metallizations or packages can greatly attenuate low-energy x rays. This is not true at higher energies. Therefore, although you might match the "free-field" dose (dose in an isolated piece of silicon), the dose in the packaged silicon deep in the system might be very different. A comparison of the dose profile in the packaged device and/or system for both the experimental and working environment will indicate if this complication exists.

2.2 Shielding Calculations

In many cases you may want to collimate the beam to protect other devices or cables from exposure to x-rays. This is often done with high-atomic-number (high-Z) shielding. Radiation transport codes can be used to design the appropriate shield materials and thicknesses. People frequently use photon attenuation tables for this, and this is not a bad first cut at the problem. However, as the bremsstrahlung is attenuated, the spectrum changes, and therefore a decrease in fluence does not translate simply into decrease in dose. A simple calculation for the geometry shown in Figure 6 will give not only the change in spectrum (Figure 7), but also the decrease in fluence and dose (Table 2). In the problem shown here we use the SPHINX spectrum shown in Figure 5, 5-cm of lead shielding, CaF_2 thermoluminescent dosimeters (TLDs) [16], and 250-µm aluminum equilibrators.

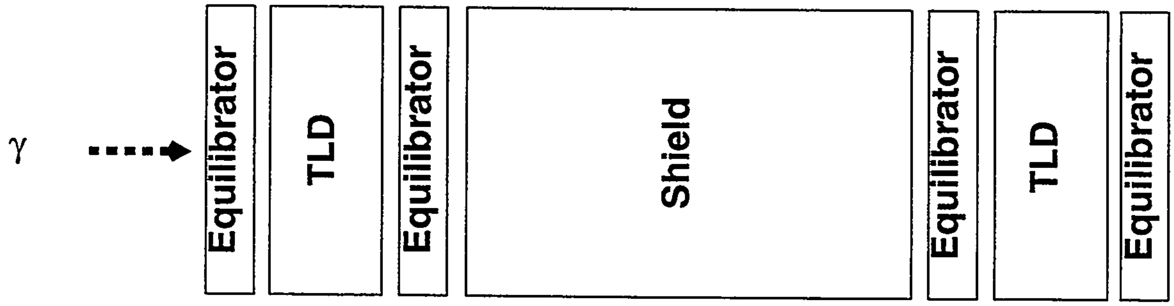

Figure 6: Schematic of model used to calculate the change in spectrum, fluence, and dose from a shield.

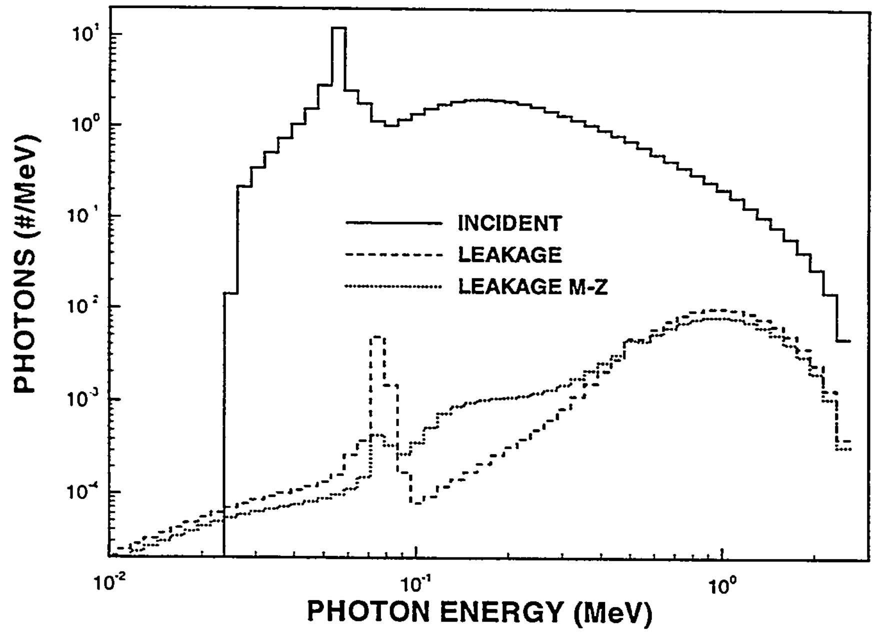

Figure 7: Plot of differential number spectra incident on and leaking from the shield geometry (lead and multi-Z shield (M-Z)) shown in Figure 6.

Table 2: Transmission of SPHINX Spectrum through Shield[a]

Shield	Number Fluence	Energy Fluence	TLD Dose
Lead	1.2%	3.2%	2.7%
Multi-Z	0.99%	2.7%	2.1%

a. We define the transmission here as the ratio of the post-shield value to the pre-shield value.

The change in spectrum shown in Figure 7 illustrates the drastic change in spectrum and the presence of the lead fluorescence line in the leakage spectrum. This spectrum change accounts for the differences shown in Table 2. The number fluence is the lowest value because the low energy photons which contain less of the energy are removed. However, a higher average energy beam, the leakage spectrum, is less efficient in depositing dose. This is why the TLD dose value is less than the energy fluence transmission.

One problem with using lead shielding is the lead fluorescence. These lower energy photons can often be a significant fraction of the dose in the components and cause dose enhancement and box IEMP response in cables. The lead lines can be easily eliminated by using a multi-Z shield to reduce the fluorescence from the shield. The geometry is the same as that shown in Figure 6 except that 3-mm of copper and 25-µm of aluminum have been added to the down stream side of the shield, forming a Pb/Cu/Al sandwich, to reduce the fluorescence emission. The resulting spectra are shown in Figure 7 and transmission values in Table 2. Note that for only 10% increase in thickness we have dropped the energy fluence by 16% and the dose by 22%. The majority of the additional attenuation is at the lowest energies where dose enhancement and box IEMP are most severe.

It is important to remember that cracks, seams, tapped holes, etc., are often not modeled, but can be very important for attenuation factors greater than 100. Scattered radiation can also be very important. It may be necessary to add side and rear shielding to remove the scattered radiation, if the primary beam has been severely attenuated. Note also that the scattered radiation spectrum will often be softer than the primary beam. An example of this is shown for a ^{60}Co cell in Figure 8. A thick lead shield has been placed in front of the lead/aluminum box. Although the scattered radiation coming in from the sides and rear were probably negligible compared to that impinging from the front when this thick shield was not present, this assumption is clearly questionable with the shield in place. Although dosimetry used in the test will accurately reflect the dose in the dosimeter, the spectrum could be very different and therefore alter the dose relative to the device due to changes in attenuation and dose enhancement. Remember that dose enhancement is not zero even when using the ASTM standard box we discussed earlier. Shielding the box on all sides with a comparable thick shield or at least increasing the shielding with the multi-Z shield to remove dose-enhancement can ameliorate this problem.

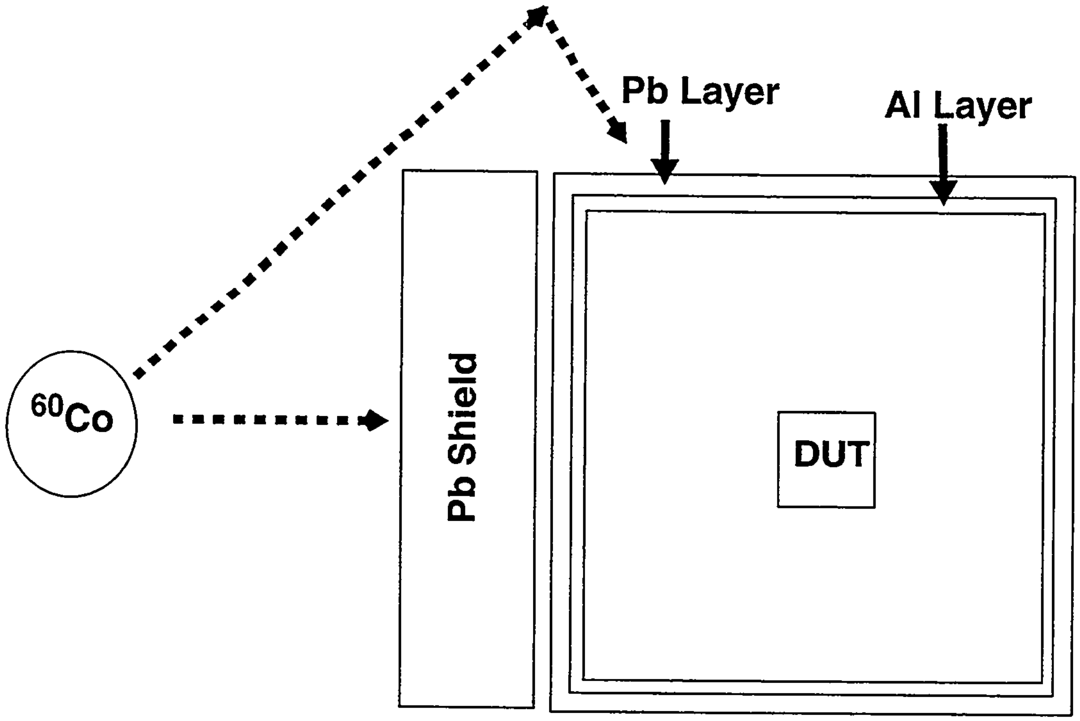

Figure 8: Schematic of ^{60}Co irradiation using thick lead shield with DUT surrounded by the standard lead/aluminum box.

2.3 Dose in the Dosimeter

If you know the incident spectrum, geometry, and materials for the dosimeter and fixturing, the calculation is relatively straightforward. The geometry is shown in Figure 9 and the CEPXS/ONELD output is shown in Table 3. We have assumed that the fixture has a 0.76-mm aluminum window and a multi-Z cable shield as discussed previously and the SPHINX x-ray spectrum is used.

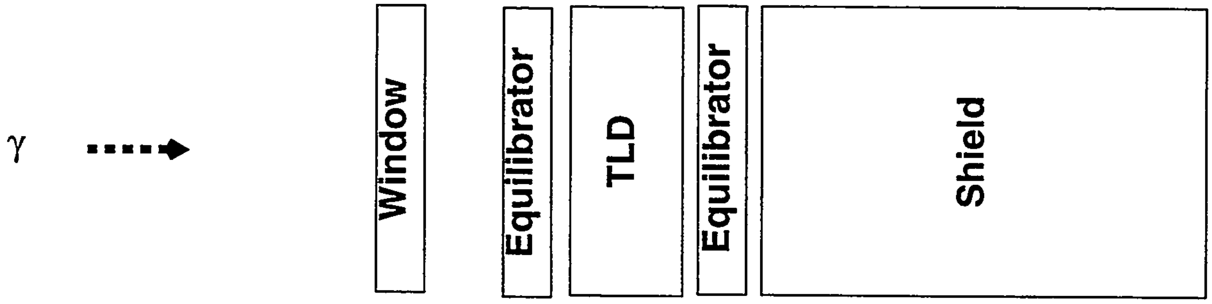

Figure 9: Schematic of model used to calculate the dose in TLD in the experiment fixture for the SPHINX x-ray spectrum.

The dose units used in CEPXS/ONELD, which are typical of many codes, are given as MeV-cm^2/g. Many people find these units quite confusing. Part of the confusion arises because in 1-D, strictly speaking, the other two dimensions do not exist. Assumptions must be made to permit the modeling of a 3-D geometry with a 1-D calculation. Different interpretations, requiring different assumptions, are possible. Users who regularly use one particular interpretation often have difficulty understanding one differing from their routine. In radiation testing, it is common to think of the source in terms of a fluence of 1 particle (photon or electron) per cm^2. Here, it is assumed (1) the source is large compared to the irradiated geometry in the other two dimensions, and either (2) the geometry is so large in extent in the other 2 dimensions that edge losses are insignificant, or (3) the area of interest is a small section of the same material also irradiated by the source, such that the side leakages sum to zero. In this case, the dose should be regarded as (MeV/g) /(#/cm^2), that is, dose per unit number fluence. (I use the term number fluence to distinguish it from the more typical energy fluence given often in units of cal/cm^2.)

For modeling pencil beams, the source should be thought of as 1 particle (photon or electron). It is assumed the geometry is large enough to capture all the significant scattered radiation. The output should then be interpreted as MeV/(g/cm^2), that is, energy deposited per thickness given in terms of areal density (thickness • mass-density).

The conversion from MeV/g to Gray is

$$1\ \text{MeV/g} = 1.602 \times 10^{-10}\ \text{Gy} = 1.602 \times 10^{-8}\ \text{rad}. \tag{3}$$

Of course to predict the dose seen in the working or experiment environment you need to know the incident fluence. This may not be known at the flash x-ray facility. If it is known, it is probably in terms of an energy fluence. Fortunately, CEPXS/ONELD gives you the average energy of the incident particle in the output in units of MeV and

$$1\ \text{MeV} = 3.829 \times 10^{-14}\ \text{cal}. \tag{4}$$

If you divide the dose by the average energy in calories, you will obtain the dose in rad/cal/cm^2, which can be used to predict the dose in the dosimeter for a given incident fluence.

Of course the dose we are referring to is the dose in the dosimeter, which, unless you are using a silicon dosimeter, is not dose silicon. If you want to convert the dose in the dosimeter to dose silicon, you must do another calculation. Replace the dosimeter and buffer with an equivalent mass thickness of silicon and appropriate buffer and rerun the calculation. (Buffers or equilibrators are often chosen to create an equilibrium environment in the material of interest. A good choice of material and thickness for the dosimeter buffer may not be the same as for silicon buffer.) This will give you the dose in silicon. The ratio of these two calculated doses gives you the conversion factor from the dosimeter dose to dose in silicon at that location. For example, for the case of Figure 9, the ratio of dose silicon to dose TLD is 0.92. Thus you can now predict the dose or dose-rate (silicon) in the fixture and convert the measured TLD doses to silicon doses.

$$D_{FFSi} = Calculated\left(\frac{D_{FFSi}}{D_{Dosimeter}}\right) \times D_{Dosimeter}, \tag{5}$$

where $D_{dosimeter}$ is the dose in the TLD and D_{FFSi} is the free-field silicon dose. Remember that this conversion factor is only good for a particular spectrum and geometry.

Table 3: Output of Transport Calculation of Dose in the Dosimeter

```
**********************************************************************      ADEPT version of CEPXS/ONELD
*                                               *                            Automatic Discretization Electron Photon
*         INPUT TO ADEPT  (MAR 13, 1992)                         *           Transport
*                                               *
**********************************************************************      copy of input deck
                                                                             number of lines in title
TITLE 2                                                                      title
Dose in CaF2 in experiment fixture for SPHINX
DOSIMETRY:  .010 AL, .035 CaF2, .020 AL                                      minimum energy used 0.001 MeV
CUTOFF 0.001
************************ MATERIALS ************************                 materials listed by standard abbreviations
MATERIAL Al                                                                  standard densities assumed for elements
MATERIAL Ca .5133 F .4867
 DENSITY 3.18
MATERIAL Pb
MATERIAL Cu
************************ GEOMETRY *************************
* MAT NZONE THICK ECUT PTCZ
GEOMETRY 7                                                                   number of layers
1 10 7.62E-2                                                                 material index, number of subzones,
1 20 2.54E-2 10                                                              thickness in cm, and number of
2 30 8.89E-2 10                                                              logarithmic subzones near interface
1 20 2.54E-2 10
1 10 2.54E-3
4 10 0.3
3 20 1.0
* PHOTON SPECTRUM FOR sphinx.pin
* MEAN PHOTON ENERGY =  4.34E-01 MeV
* ENERGY INTEGRAL    =  1.9458E-01
PHOTON-SOURCE                                                                photon source
SPECTRUM 43                                                                  number of bins in spectrum
 1.000000  .998665  .994374  .987104  .976911  .963840  .947912  .929152     fraction of photons below an energy
  .907536  .883109  .855863  .825835  .793075  .757664  .719705  .679164
  .636664  .592275  .546361  .499360  .451871  .404569  .358469  .314765
  .274606  .238978  .208621  .183753  .164196  .149350  .138291  .130067
```

Table 3: Output of Transport Calculation of Dose in the Dosimeter Continued

```
 .116721  .099161  .098643  .059114  .026440  .014407  .007965  .004176
 .001955  .000681  .000000
ENERGIES                                                                     the energy bins for the spectrum
 2.613000 2.328500 2.075100 1.849200 1.647900 1.468500 1.308600 1.166200
 1.039200  .926090  .825270  .735430  .655370  .584030  .520450  .463800
  .413310  .368310  .328220  .292490  .260650  .232270  .206990  .184460
  .164380  .146480  .130540  .116330  .103660  .092378  .082322  .073360
  .065374  .058258  .058033  .057033  .051916  .046264  .041228  .036740
  .032740  .029176  .026000
output                                                                       output options follow
edep                                                                         energy deposition requested



************************************************************************
*                                                  *
*           PROBLEM DEFINITION                                 *            Output
*                                                  *
************************************************************************

  LAYER     THICKNESS     MATERIAL     DENSITY                               list of materials and densities used

    1       7.6200E-02       1        2.7000E+00
    2       2.5400E-02       1        2.7000E+00
    3       8.8900E-02       2        3.1800E+00
    4       2.5400E-02       1        2.7000E+00
    5       2.5400E-03       1        2.7000E+00
    6       3.0000E-01       4        8.9600E+00
    7       1.0000E+00       3        1.1400E+01

Plane-Wave at Angle of Incidence =  8.3494E+00 Degrees                       average angle of normal incidence bin
Default Electron Groups =  71                                                number of electron groups
Default Photon Groups =  71                                                  number of photon groups
Default SN Order = 16                                                        number of angle groups
```

Table 3: Output of Transport Calculation of Dose in the Dosimeter Continued

```
1************************************************************************
*                                          *
*              OUTPUT (IBM)                      *
*                                          *
*        AVERAGE SOURCE ENERGY =  4.3362E-01 MeV          *
*                                          *
*       ALL QUANTITIES NORMALIZED TO A SINGLE SOURCE PARTICLE   *
*                                          *
*     FOR A SLAB, THIS IS THE SAME AS NORMALIZING TO A          *
*     UNIT NUMBER FLUX (SOURCE PARTICLES/CM2)             *
*                                          *
*     NO PAIR SECONDARIES PRODUCED                       *
*                                          *
*   SPATIAL MESH AND GROUP STRUCTURE OPTIMIZED FOR    DOSE        *
*                                          *
************************************************************************

  LAYER    MASS-THICKNESS      DOSE DEPOSITION
             (g/cm2)          (MeV-cm2/g)

    1       2.0574E-01        1.0777E-02
    2       6.8580E-02        1.3124E-02
    3       2.8270E-01        1.5819E-02
    4       6.8580E-02        1.4367E-02
    5       6.8580E-03        1.8731E-02
    6       2.6880E+00         1.9749E-02
    7       1.1400E+01         1.9857E-02

TOTAL ENERGY DEPOSITED =   2.8816E-01 MeV/source

************************************************************************
```

AIX IBM version

average energy of source
This number is useful for converting to numbers normalized to energy fluence.

Not important at low energies and was disabled. Energy is deposited but particles not transported.
OK, because electron currents not selected.

mass thickness is the same as areal density

dose deposited in each layer, can be easily converted to Gy or rad

Table 3: Output of Transport Calculation of Dose in the Dosimeter Continued

```
RESIDENT KERMA (DERIVED FROM PHOTON-FIELD ONLY)

 LAYER    MATERIAL    DOSE (MeV-cm2/g)

  1        1       1.3760E-02
  2        1       1.3721E-02
  3        2       1.5862E-02
  4        1       1.3461E-02
  5        1       1.3489E-02
  6        4       1.9433E-02
  7        3       2.0024E-02
```

This is the equilibrium dose that would have been deposited in the layer from the photon fluence. Note that it is assumed that none of the bremsstrahlung from secondary electrons is absorbed in the layer in which it is created. Therefore, it is subtracted from the kerma, so that this quantity is equal to the equilibrium dose, especially at high energies where bremsstrahlung is significant.

```
*************************************************************************

ENERGY CONSERVATION RATIO =  1.0028E+00
```

should be very close to 1, if not, results are suspect

```
 LAYER   CHARGED-PARTICLE CONSERVATION RATIO

  1       1.0000E+00
  2       1.0001E+00
  3       9.9997E-01
  4       1.0001E+00
  5       9.9997E-01
  6       1.0000E+00
  7       1.0000E+00


*************************************************************************
```

should be very close to 1, if not, results are suspect

```
DIFFERENTIAL DOSE PROFILE

    x (cm)       dose(MeV-cm2/g)   Mesh(g/cm2)   Material  Layer
```

dose in each spatial element
material and layer index are identified for each spatial element or subzone

Table 3: Output of Transport Calculation of Dose in the Dosimeter Continued

```
3.81000000E-03   6.031331E-03   2.057400E-02   1   1
1.14300000E-02   8.736321E-03   2.057400E-02   1   1
1.90500000E-02   9.876404E-03   2.057400E-02   1   1
2.66700000E-02   1.065960E-02   2.057400E-02   1   1
3.42900000E-02   1.122955E-02   2.057400E-02   1   1
4.19100001E-02   1.166759E-02   2.057400E-02   1   1
4.95300001E-02   1.201510E-02   2.057400E-02   1   1
5.71500001E-02   1.229721E-02   2.057400E-02   1   1
6.47700001E-02   1.253075E-02   2.057400E-02   1   1
7.23900001E-02   1.272811E-02   2.057400E-02   1   1
7.62004624E-02   1.281781E-02   2.496690E-06   1   2
7.62018839E-02   1.281783E-02   5.179410E-06   1   2
7.62048329E-02   1.281788E-02   1.074519E-05   1   2
7.62109510E-02   1.281801E-02   2.229228E-05   1   2
7.62236436E-02   1.281828E-02   4.624803E-05   1   2
7.62499760E-02   1.281886E-02   9.594666E-05   1   2
7.63046053E-02   1.282006E-02   1.990518E-04   1   2
7.64179399E-02   1.282258E-02   4.129550E-04   1   2
7.66530652E-02   1.282781E-02   8.567216E-04   1   2
7.71408587E-02   1.283862E-02   1.777363E-03   1   2
7.81050001E-02   1.285978E-02   3.429000E-03   1   2
7.93750001E-02   1.288727E-02   3.429000E-03   1   2
8.06450001E-02   1.291436E-02   3.429000E-03   1   2
8.19150001E-02   1.294110E-02   3.429000E-03   1   2
8.31850001E-02   1.296759E-02   3.429000E-03   1   2
8.44550001E-02   1.299392E-02   3.429000E-03   1   2
8.57250001E-02   1.302020E-02   3.429000E-03   1   2
8.69950001E-02   1.304657E-02   3.429000E-03   1   2
8.82650001E-02   1.307322E-02   3.429000E-03   1   2
8.95350000E-02   1.310039E-02   3.429000E-03   1   2
9.08050000E-02   1.312838E-02   3.429000E-03   1   2
9.20750000E-02   1.315765E-02   3.429000E-03   1   2
9.33450000E-02   1.318886E-02   3.429000E-03   1   2
9.46150000E-02   1.322306E-02   3.429000E-03   1   2
9.58850000E-02   1.326196E-02   3.429000E-03   1   2
```

These data are good for obtaining depth-dose profiles.

Table 3: Output of Transport Calculation of Dose in the Dosimeter Continued

```
9.71550000E-02   1.330867E-02   3.429000E-03   1   2
9.84250000E-02   1.336932E-02   3.429000E-03   1   2
9.96950000E-02   1.346064E-02   3.429000E-03   1   2
1.00659141E-01   1.360254E-02   1.777364E-03   1   2
1.01146935E-01   1.378526E-02   8.567208E-04   1   2
1.01382060E-01   1.394880E-02   4.129542E-04   1   2
1.01495394E-01   1.405889E-02   1.990521E-04   1   2
1.01550024E-01   1.412271E-02   9.594720E-05   1   2
1.01576356E-01   1.415738E-02   4.624830E-05   1   2
1.01589049E-01   1.419715E-02   2.229120E-05   1   2
1.01595167E-01   1.424553E-02   1.074600E-05   1   2
1.01598116E-01   1.426216E-02   5.181300E-06   1   2
1.01599538E-01   1.419940E-02   2.494800E-06   1   2
1.01600376E-01   1.473986E-02   2.391360E-06   2   3                TLD is layer 3
1.01601640E-01   1.467415E-02   5.647680E-06   2   3
1.01604622E-01   1.469913E-02   1.332102E-05   2   3
1.01611660E-01   1.475519E-02   3.143748E-05   2   3
1.01628269E-01   1.479793E-02   7.419894E-05   2   3
1.01667467E-01   1.486788E-02   1.750972E-04   2   3
1.01759971E-01   1.501783E-02   4.132315E-04   2   3
1.01978280E-01   1.528206E-02   9.752138E-04   2   3
1.02493482E-01   1.558284E-02   2.301468E-03   2   3
1.03709341E-01   1.574205E-02   5.431395E-03   2   3
1.06045001E-01   1.579790E-02   9.423400E-03   2   3
1.09008334E-01   1.581745E-02   9.423400E-03   2   3
1.11971667E-01   1.582254E-02   9.423400E-03   2   3
1.14935001E-01   1.582477E-02   9.423400E-03   2   3
1.17898334E-01   1.582631E-02   9.423400E-03   2   3
1.20861667E-01   1.582759E-02   9.423400E-03   2   3
1.23825001E-01   1.582862E-02   9.423400E-03   2   3
1.26788334E-01   1.582939E-02   9.423400E-03   2   3
1.29751667E-01   1.582991E-02   9.423400E-03   2   3
1.32715001E-01   1.583019E-02   9.423400E-03   2   3
1.35678334E-01   1.583027E-02   9.423400E-03   2   3
1.38641667E-01   1.583018E-02   9.423400E-03   2   3
```

Table 3: Output of Transport Calculation of Dose in the Dosimeter Continued

1.41605001E-01	1.582997E-02	9.423400E-03	2	3
1.44568334E-01	1.582972E-02	9.423400E-03	2	3
1.47531667E-01	1.582951E-02	9.423400E-03	2	3
1.50495000E-01	1.582942E-02	9.423400E-03	2	3
1.53458334E-01	1.582957E-02	9.423400E-03	2	3
1.56421667E-01	1.583007E-02	9.423400E-03	2	3
1.59385000E-01	1.583106E-02	9.423400E-03	2	3
1.62348334E-01	1.583267E-02	9.423400E-03	2	3
1.65311667E-01	1.583504E-02	9.423400E-03	2	3
1.68275000E-01	1.583831E-02	9.423400E-03	2	3
1.71238334E-01	1.584257E-02	9.423400E-03	2	3
1.74201667E-01	1.584778E-02	9.423400E-03	2	3
1.77165000E-01	1.585356E-02	9.423400E-03	2	3
1.80128334E-01	1.585866E-02	9.423400E-03	2	3
1.83091667E-01	1.585920E-02	9.423400E-03	2	3
1.86055000E-01	1.583993E-02	9.423400E-03	2	3
1.88390659E-01	1.577546E-02	5.431392E-03	2	3
1.89606518E-01	1.565263E-02	2.301471E-03	2	3
1.90121720E-01	1.546717E-02	9.752106E-04	2	3
1.90340028E-01	1.529660E-02	4.132315E-04	2	3
1.90432533E-01	1.519289E-02	1.751003E-04	2	3
1.90471731E-01	1.514222E-02	7.419576E-05	2	3
1.90488340E-01	1.510779E-02	3.144066E-05	2	3
1.90495378E-01	1.505807E-02	1.332102E-05	2	3
1.90498360E-01	1.503756E-02	5.644500E-06	2	3
1.90499624E-01	1.510703E-02	2.391360E-06	2	3
1.90500462E-01	1.455423E-02	2.497500E-06	1	4
1.90501884E-01	1.462163E-02	5.178600E-06	1	4
1.90504833E-01	1.461003E-02	1.074600E-05	1	4
1.90510951E-01	1.456835E-02	2.229120E-05	1	4
1.90523643E-01	1.453521E-02	4.624830E-05	1	4
1.90549976E-01	1.450675E-02	9.594720E-05	1	4
1.90604605E-01	1.444924E-02	1.990521E-04	1	4
1.90717940E-01	1.434184E-02	4.129542E-04	1	4
1.90953065E-01	1.416581E-02	8.567235E-04	1	4

Table 3: Output of Transport Calculation of Dose in the Dosimeter Continued

```
 1.91440859E-01    1.395453E-02    1.777361E-03   1   4
 1.92405000E-01    1.383238E-02    3.429000E-03   1   4
 1.93675000E-01    1.381642E-02    3.429000E-03   1   4
 1.94945000E-01    1.383170E-02    3.429000E-03   1   4
 1.96215000E-01    1.385957E-02    3.429000E-03   1   4
 1.97485000E-01    1.389584E-02    3.429000E-03   1   4
 1.98755000E-01    1.393844E-02    3.429000E-03   1   4
 2.00025000E-01    1.398668E-02    3.429000E-03   1   4
 2.01295000E-01    1.404057E-02    3.429000E-03   1   4
 2.02565000E-01    1.410064E-02    3.429000E-03   1   4
 2.03835000E-01    1.416792E-02    3.429000E-03   1   4
 2.05105000E-01    1.424395E-02    3.429000E-03   1   4
 2.06375000E-01    1.433099E-02    3.429000E-03   1   4
 2.07645000E-01    1.443233E-02    3.429000E-03   1   4
 2.08915000E-01    1.455285E-02    3.429000E-03   1   4
 2.10185000E-01    1.470009E-02    3.429000E-03   1   4
 2.11455000E-01    1.488632E-02    3.429000E-03   1   4
 2.12725000E-01    1.513278E-02    3.429000E-03   1   4
 2.13995000E-01    1.547961E-02    3.429000E-03   1   4
 2.14959141E-01    1.584434E-02    1.777364E-03   1   4
 2.15446935E-01    1.608771E-02    8.567208E-04   1   4
 2.15682060E-01    1.622492E-02    4.129569E-04   1   4
 2.15795395E-01    1.629665E-02    1.990521E-04   1   4
 2.15850024E-01    1.633264E-02    9.594450E-05   1   4
 2.15876356E-01    1.635032E-02    4.624830E-05   1   4
 2.15889049E-01    1.635890E-02    2.229390E-05   1   4
 2.15895167E-01    1.636304E-02    1.074330E-05   1   4
RESIDENT DIFFERENTIAL KERMA PROFILE
DOSE DERIVED FROM PHOTON-FIELD ONLY

   x (cm)        dose (MeV-cm2/g)   Mesh(g/cm2)  Material  Layer

 3.81000000E-03    1.376873E-02    2.057400E-02   1   1
 1.14300000E-02    1.377163E-02    2.057400E-02   1   1
 1.90500000E-02    1.377116E-02    2.057400E-02   1   1
```

equilibrium dose in each spatial element material and layer index are identified for each spatial element or subzone

When compared to the dose profile, this can be used to indicate the amount of dose enhancement in a material. Because dose

Table 3: Output of Transport Calculation of Dose in the Dosimeter Continued

```
2.66700000E-02    1.376925E-02    2.057400E-02   1   1
3.42900000E-02    1.376621E-02    2.057400E-02   1   1
4.19100001E-02    1.376223E-02    2.057400E-02   1   1
4.95300001E-02    1.375739E-02    2.057400E-02   1   1
5.71500001E-02    1.375178E-02    2.057400E-02   1   1
6.47700001E-02    1.374542E-02    2.057400E-02   1   1
7.23900001E-02    1.373836E-02    2.057400E-02   1   1
7.62004624E-02    1.373460E-02    2.496690E-06   1   2
7.62018839E-02    1.373460E-02    5.179410E-06   1   2
7.62048329E-02    1.373460E-02    1.074519E-05   1   2
7.62109510E-02    1.373459E-02    2.229228E-05   1   2
7.62236436E-02    1.373458E-02    4.624803E-05   1   2
7.62499760E-02    1.373455E-02    9.594666E-05   1   2
7.63046053E-02    1.373450E-02    1.990518E-04   1   2
7.64179399E-02    1.373438E-02    4.129550E-04   1   2
7.66530652E-02    1.373414E-02    8.567216E-04   1   2
7.71408587E-02    1.373364E-02    1.777363E-03   1   2
7.81050001E-02    1.373264E-02    3.429000E-03   1   2
7.93750001E-02    1.373132E-02    3.429000E-03   1   2
8.06450001E-02    1.372997E-02    3.429000E-03   1   2
8.19150001E-02    1.372860E-02    3.429000E-03   1   2
8.31850001E-02    1.372722E-02    3.429000E-03   1   2
8.44550001E-02    1.372582E-02    3.429000E-03   1   2
8.57250001E-02    1.372439E-02    3.429000E-03   1   2
8.69950001E-02    1.372295E-02    3.429000E-03   1   2
8.82650001E-02    1.372149E-02    3.429000E-03   1   2
8.95350000E-02    1.372002E-02    3.429000E-03   1   2
9.08050000E-02    1.371852E-02    3.429000E-03   1   2
9.20750000E-02    1.371701E-02    3.429000E-03   1   2
9.33450000E-02    1.371547E-02    3.429000E-03   1   2
9.46150000E-02    1.371393E-02    3.429000E-03   1   2
9.58850000E-02    1.371237E-02    3.429000E-03   1   2
9.71550000E-02    1.371084E-02    3.429000E-03   1   2
9.84250000E-02    1.370947E-02    3.429000E-03   1   2
9.96950000E-02    1.370900E-02    3.429000E-03   1   2
```

enhancement takes place near the interface, it often is not observable for thick layers unless the profile is examined and has an adequate number of zones in the layer. For example, two zones in the TLD would not be sufficient.

Table 3: Output of Transport Calculation of Dose in the Dosimeter Continued

```
1.00659141E-01    1.371098E-02    1.777364E-03    1    2
1.01146935E-01    1.371469E-02    8.567208E-04    1    2
1.01382060E-01    1.371807E-02    4.129542E-04    1    2
1.01495394E-01    1.372037E-02    1.990521E-04    1    2
1.01550024E-01    1.372157E-02    9.594720E-05    1    2
1.01576356E-01    1.372196E-02    4.624830E-05    1    2
1.01589049E-01    1.372198E-02    2.229120E-05    1    2
1.01595167E-01    1.372193E-02    1.074600E-05    1    2
1.01598116E-01    1.372188E-02    5.181300E-06    1    2
1.01599538E-01    1.372185E-02    2.494800E-06    1    2
1.01600376E-01    1.608915E-02    2.391360E-06    2    3                TLD is layer 3
1.01601640E-01    1.608866E-02    5.647680E-06    2    3
1.01604622E-01    1.608767E-02    1.332102E-05    2    3
1.01611660E-01    1.608604E-02    3.143748E-05    2    3
1.01628269E-01    1.608418E-02    7.419894E-05    2    3
1.01667467E-01    1.608327E-02    1.750972E-04    2    3
1.01759971E-01    1.608464E-02    4.132315E-04    2    3
1.01978280E-01    1.608850E-02    9.752138E-04    2    3
1.02493482E-01    1.609158E-02    2.301468E-03    2    3
1.03709341E-01    1.608809E-02    5.431395E-03    2    3
1.06045001E-01    1.607594E-02    9.423400E-03    2    3
1.09008334E-01    1.605998E-02    9.423400E-03    2    3
1.11971667E-01    1.604416E-02    9.423400E-03    2    3
1.14935001E-01    1.602844E-02    9.423400E-03    2    3
1.17898334E-01    1.601277E-02    9.423400E-03    2    3
1.20861667E-01    1.599713E-02    9.423400E-03    2    3
1.23825001E-01    1.598151E-02    9.423400E-03    2    3
1.26788334E-01    1.596589E-02    9.423400E-03    2    3
1.29751667E-01    1.595025E-02    9.423400E-03    2    3
1.32715001E-01    1.593461E-02    9.423400E-03    2    3
1.35678334E-01    1.591894E-02    9.423400E-03    2    3
1.38641667E-01    1.590324E-02    9.423400E-03    2    3
1.41605001E-01    1.588751E-02    9.423400E-03    2    3
1.44568334E-01    1.587174E-02    9.423400E-03    2    3
1.47531667E-01    1.585593E-02    9.423400E-03    2    3
```

Table 3: Output of Transport Calculation of Dose in the Dosimeter Continued

1.50495000E-01	1.584007E-02	9.423400E-03	2	3
1.53458334E-01	1.582416E-02	9.423400E-03	2	3
1.56421667E-01	1.580820E-02	9.423400E-03	2	3
1.59385000E-01	1.579219E-02	9.423400E-03	2	3
1.62348334E-01	1.577612E-02	9.423400E-03	2	3
1.65311667E-01	1.575999E-02	9.423400E-03	2	3
1.68275000E-01	1.574380E-02	9.423400E-03	2	3
1.71238334E-01	1.572755E-02	9.423400E-03	2	3
1.74201667E-01	1.571125E-02	9.423400E-03	2	3
1.77165000E-01	1.569493E-02	9.423400E-03	2	3
1.80128334E-01	1.567861E-02	9.423400E-03	2	3
1.83091667E-01	1.566239E-02	9.423400E-03	2	3
1.86055000E-01	1.564643E-02	9.423400E-03	2	3
1.88390659E-01	1.563372E-02	5.431392E-03	2	3
1.89606518E-01	1.562474E-02	2.301471E-03	2	3
1.90121720E-01	1.561692E-02	9.752106E-04	2	3
1.90340028E-01	1.561145E-02	4.132315E-04	2	3
1.90432533E-01	1.560966E-02	1.751003E-04	2	3
1.90471731E-01	1.561053E-02	7.419576E-05	2	3
1.90488340E-01	1.561243E-02	3.144066E-05	2	3
1.90495378E-01	1.561410E-02	1.332102E-05	2	3
1.90498360E-01	1.561511E-02	5.644500E-06	2	3
1.90499624E-01	1.561562E-02	2.391360E-06	2	3
1.90500462E-01	1.348716E-02	2.497500E-06	1	4
1.90501884E-01	1.348720E-02	5.178600E-06	1	4
1.90504833E-01	1.348725E-02	1.074600E-05	1	4
1.90510951E-01	1.348732E-02	2.229120E-05	1	4
1.90523643E-01	1.348732E-02	4.624830E-05	1	4
1.90549976E-01	1.348697E-02	9.594720E-05	1	4
1.90604605E-01	1.348579E-02	1.990521E-04	1	4
1.90717940E-01	1.348344E-02	4.129542E-04	1	4
1.90953065E-01	1.347972E-02	8.567235E-04	1	4
1.91440859E-01	1.347498E-02	1.777361E-03	1	4
1.92405000E-01	1.347065E-02	3.429000E-03	1	4
1.93675000E-01	1.346786E-02	3.429000E-03	1	4

Table 3: Output of Transport Calculation of Dose in the Dosimeter Continued

```
1.94945000E-01   1.346595E-02   3.429000E-03   1   4
1.96215000E-01   1.346425E-02   3.429000E-03   1   4
1.97485000E-01   1.346263E-02   3.429000E-03   1   4
1.98755000E-01   1.346108E-02   3.429000E-03   1   4
2.00025000E-01   1.345963E-02   3.429000E-03   1   4
2.01295000E-01   1.345828E-02   3.429000E-03   1   4
2.02565000E-01   1.345707E-02   3.429000E-03   1   4
2.03835000E-01   1.345602E-02   3.429000E-03   1   4
2.05105000E-01   1.345519E-02   3.429000E-03   1   4
2.06375000E-01   1.345462E-02   3.429000E-03   1   4
2.07645000E-01   1.345438E-02   3.429000E-03   1   4
2.08915000E-01   1.345456E-02   3.429000E-03   1   4
2.10185000E-01   1.345530E-02   3.429000E-03   1   4
2.11455000E-01   1.345675E-02   3.429000E-03   1   4
2.12725000E-01   1.345917E-02   3.429000E-03   1   4
2.13995000E-01   1.346298E-02   3.429000E-03   1   4
2.14959141E-01   1.346713E-02   1.777364E-03   1   4
2.15446935E-01   1.346988E-02   8.567208E-04   1   4
2.15682060E-01   1.347141E-02   4.129569E-04   1   4
2.15795395E-01   1.347221E-02   1.990521E-04   1   4
2.15850024E-01   1.347261E-02   9.594450E-05   1   4
2.15876356E-01   1.347280E-02   4.624830E-05   1   4
2.15889049E-01   1.347290E-02   2.229390E-05   1   4
```

These calculations can also give very important information about experiment design. There are two important questions you should ask yourself about the dosimetry. First, is this the correct dosimeter for the test environment? The dosimeter should not only be able to give accurate measurements for the dose and dose rates expected, but also be minimally attenuating. Ideally the dose should vary less than 10% through the dosimeter. If a large fraction of the energy is absorbed in the front of the dosimeter, then the average dose measured will be far less than the peak dose. In Figure 10, the dose and equilibrium dose in the model shown in Figure 9 are plotted as a function of depth. The region of the TLD is highlighted. From Figure 10 and Table 3 it is clear that the TLD and its equilibrator attenuate the dose by less than 5%.

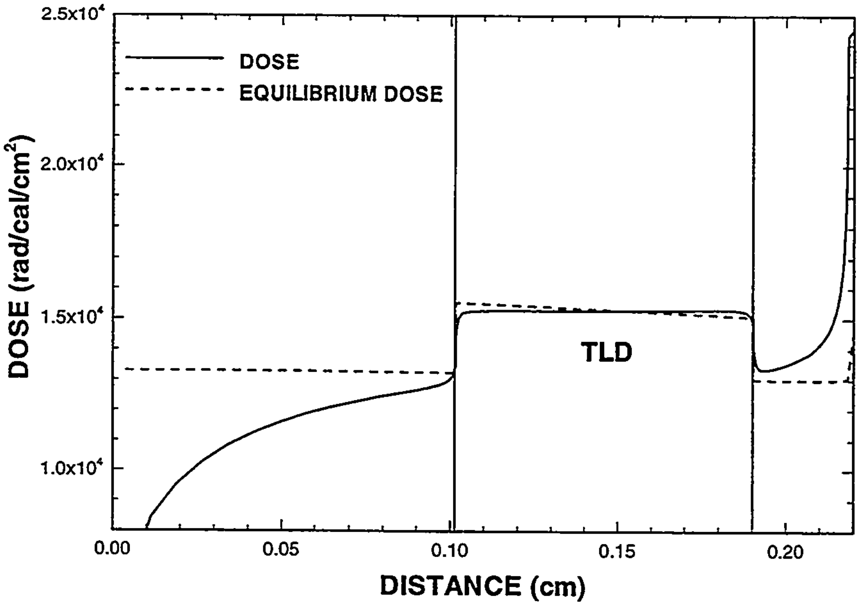

Figure 10: Plot of dose as a function of depth in the model shown in Figure 9. Note that the dose and equilibrium dose agree well in the TLD region.

Second, is this the right equilibrator or buffer for the test environment? Although combined photon/electron transport codes are excellent for predicting non-equilibrium doses, in general it is prudent to design the dosimeter to be in charged-particle equilibrium [17]. If the equilibrator is not of similar Z to the dosimeter, then the dose will not be an equilibrium dose in at least some portion (a secondary-electron range) of the dosimeter. If the equilibrator is too thin, than the dosimeter may not be in equilibrium and will be sensitive to the scattered electron environment in the test fixture. (This response can also be calculated in principle, but is not trivial [18].) If the equilibrator is too thick, then this may alter the spectrum. This can easily be checked with the dosimetry calculation shown in Table 3 and Figure 10, by examining the dose profile and the equilibrium dose profile through the equilibrator and dosimeter material. If the dose profile is relatively flat and the two profiles agree with each other, then you have a good design. If not, try changing thickness and materials to achieve this state. (Note that disagreements in the dose and equilibrium dose at the front of the upstream equilibrator are not a problem. This is the function of the equilibrator. However, they should agree immediately before the dosimeter. However, without the aluminum window of the fixture the upstream equilibrator might not be sufficient. In addition, we have ignored the secondary electrons emitted from the faceplate of the accelerator. The dose from these can be calculated [18], but it is generally best to remove them with the window/equilibrator, so they can be ignored.)

2.4 Dose in the Device

Unfortunately "real" ICs and their packaging rarely provide an equilibrium dose, and there is not much one can do to change the situation. This is why it is extremely important to use a combined electron/photon transport code. Because the secondary-electron fluence is not in equilibrium, electron transport is significant. This lack of equilibrium is also what causes dose enhancement, that is, a different dose than expected from equilibrium conditions. Because dose enhancement is very sensitive to low energy (<400 keV) spectral components, material composition and thickness, it is very important to have an accurate spectrum, and device and package description. A sample geometry is shown in Figure 11. The geometry shown is the same as used in Reference 19. We then use the SPHINX x-ray spectrum and the fixture window and shield geometry shown in Figure 9 to calculate the dose in the device. The dose and equilibrium dose profiles are shown in Figure 12. Because this is a one-dimensional representation, several different cross-sections of the device should be modeled to look for variations in dose.

Au	2.5 μm
Ni	3.0 μm
KOVAR	0.25 mm
Ni	3.0 μm
Au	2.5 μm
N_2	0.8 mm
SiO_2	1.0 μm
Al	1.0 μm
SiO_2	50 nm
Si epi	5.0 μm
Si bulk	635.0 μm
Ti	5.08 μm
Au	3.84 μm
Au Si	50.8 μm
Au	2.5 μm
W	15.2 μm
Al_2O_3	1.016 mm

Figure 11: Schematic of model used to calculate the dose in a packaged device.

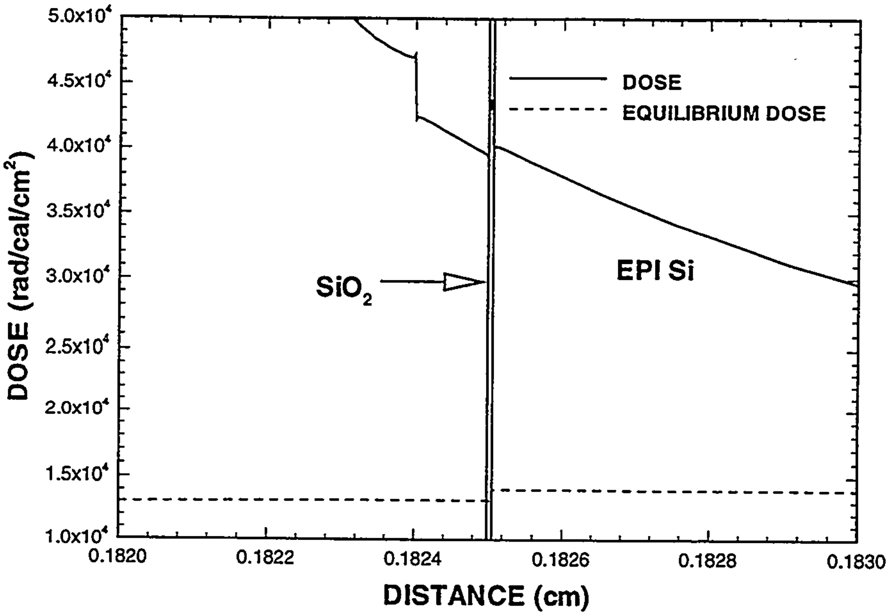

Figure 12: Plot of dose as a function of depth in the model shown in Figures 9 and 12. Note that the dose and equilibrium dose do not agree.

As with the dosimeter, it is important to exclude electrons generated outside the package. This can be determined by using the depth-dose profiles shown in Figure 10. Because the window was sufficient to reach equilibrium in the aluminum, that thickness plus the package lid is certainly sufficient to exclude external electrons for the device.

Finally, we must address the issue of dose-enhancement. As stated earlier, because the device and package are fixed, we cannot alter the dose-enhancement factors, only note them. We define the dose enhancement factor to be the ratio of the dose to the equilibrium dose. Using Figure 12 we can examine the differences in the dose and equilibrium dose profiles in the regions of interest. Clearly, we do not have charged particle equilibrium. For example, the dose-enhancement factor is 3.2 for the gate oxide region and 2.3 for the epitaxial silicon region.

2.5 Correlation of Dosimeter Dose to Device

If all that is required is to ensure that you exposed the device to a particular free-field silicon dose, Equation 5 will do the job. If your test spectrum is not a good match to the working environment or you need to know the specific dose in the device, a further calculation must be done. Now that we have performed all of these calculations it is quite easy to infer the dose in a specific device layer to the measured dose in the dosimeter. The equation is very similar to Equation 5.

$$D_{DL} = Calculated\left(\frac{D_{DL}}{D_{Dosimeter}}\right) \times D_{Dosimeter} \,, \tag{6}$$

where $D_{dosimeter}$ is the dose in the TLD and D_{DL} is the dose in a particular layer of the device. This calculated ratio includes all the effects of attenuation, mass-energy absorption differences, and dose-enhancement. Again, remember that this conversion factor is only good for a particular spectrum and geometry.

A final calculation is necessary. Using the model of the device (Figure 11), a model of the system chassis and the spectrum and fluence of the working environment, calculate the dose in the device. Compare this with the dose you obtained using Equation 6. If the doses are comparable for all the cross-sections of the device you have modeled, then you are finished. If not, then you have a simulation fidelity problem, and you will have to determine the level of overtest necessary to qualify the component. We will not deal with this problem here.

In this section we have shown a number of sample calculations and how to use them to design and analyze a radiation test on a device in a photon field. This is certainly by no means complete, but should be a good start on the type of quantities of interest and what problems may arise. When used properly these codes can be a excellent tool for experiment design. In the next two sections, we will deal briefly with the perils specific to electron and proton environments. Many of the mechanics of the calculations are the same and we will not repeat them.

3.0 Electron Irradiation

In many ways there is little difference in running calculations using an electron source instead of a photon source. For example, in CEPXS/ONELD one only needs to change the key word "photon-source" to "electron-source." The form of the spectrum input is identical. There are three key differences in electron beam sources. First, the energy of the beam changes dramatically as a function of depth in the material because of the strong interaction of the electrons. Second, there is never charged particle equilibrium or what one would call an equilibrium dose. One can attain a region where the deposition is dominated by the primary beam and exclude external low-energy secondaries, but this is not equilibrium in the photon source sense. Third, charging of the materials is a very important consideration. When the electrons stop, they will either be trapped in an insulator or follow an electrical circuit to ground or a power supply. We will deal with these key differences in this section.

Electron beams are typically used to simulate two types of environments. One is the low energy (< 5 MeV) space or reactor environment. Van de Graaff accelerators are typically used for this application. Charging of insulators is an extremely important issue here and as mentioned earlier, the time dependence of the changing electric fields must be handled with additional codes [4]. The other environment is a γ irradiation and linacs (> 10 MeV) are typically used here. High-energy electrons can be a good simulation of this environment as long as one ensures that the deposition profile is relatively flat and that charging is not an issue. In this section we will deal with the use of electron beams for γ simulation. A typical fixture is shown in Figure 13.

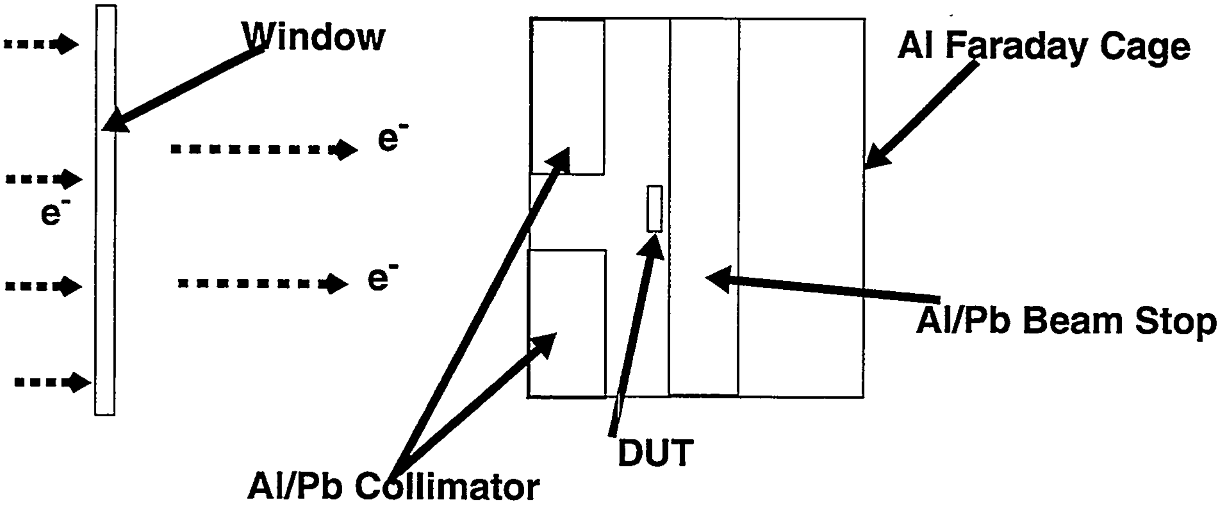

Figure 13: Schematic of linac irradiation with electrons first traversing the vacuum window on the left and then incident on the DUT in a Faraday cage with an aluminum/lead collimator and beam stop.

3.1 Electron Spectrum Calculation

The linac facility will typically tell you the energy of the electron environment. If the system is using bending magnets for energy analysis, then this is probably a fairly well defined number. If not, then the energy may depend on the how the machine is performing day to day. You may want to check the spectrum. This can be done using a process similar to that given in ASTM standard E 665 [15] and mentioned in the preceding photon section. A stack of aluminum and TLDs described in Reference 18 can provide you with an experimental depth dose profile that can be compared to a calculation of the dose profile. Agreement is a good indication that you know the electron spectrum.

Fortunately, dose-enhancement is not a major issue in high-energy electron or gamma environments. However, charge deposition and a rapidly varying deposition can be problems. Usually, the test is designed so the primary beam stops well after the dosimetry and the DUT, and that the dose profile is relatively flat within these regions. Charge deposition could give erroneous electrical measurements by introducing currents into the circuit that would not be there. A rapidly varying dose profile can give you a more uncertainty in the dose if you don't know the beam energy or material thicknesses well. The higher the electron energy, the flatter the dose profile and the deeper the beam will penetrate before depositing its charge. Of course, higher electron energy beams induce a greater activation in the materials. This is a trade off you must consider. (I like 25-40 MeV electron beams.) In Figures 14 and 15 we plot the energy and charge deposition as a function of depth in aluminum for 10-,20-, and 30-MeV electrons. For a 20-MeV electron beam the best place to make measurements is within the equivalent of the first cm of aluminum but have at least a 1-mm aluminum-equivalent thickness in front to avoid charge deposition problems. Note that, for 10-MeV electrons, both the dose and charge profiles vary rapidly with depth, and small changes in geometry can be very important. In the regions of high charge deposition, the materials should be well grounded metals, so as not to cause charging and measurement circuit problems. Of course, you need to model the TLD and DUT to obtain the right thicknesses of material and to relate their doses.

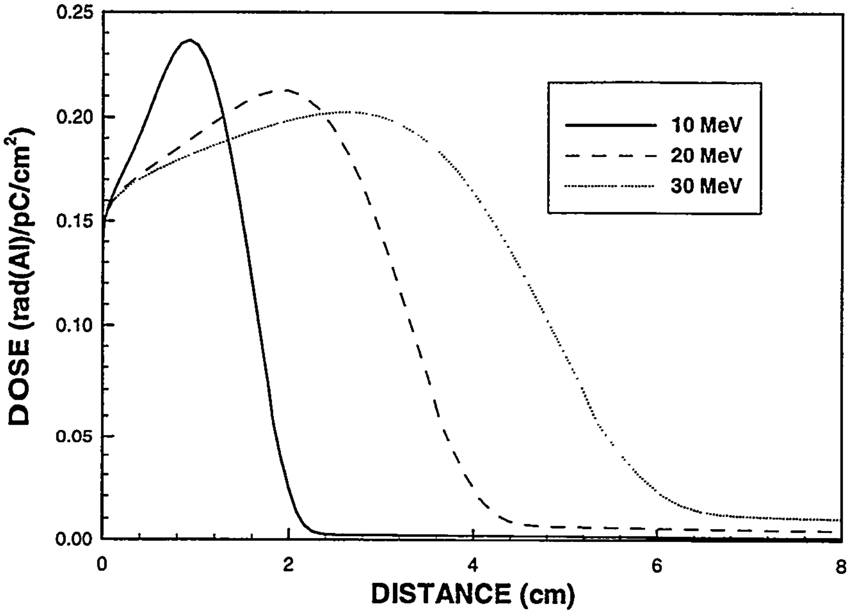

Figure 14: Plot of dose as a function of distance in aluminum for 10-, 20-, and 30-MeV electron beams.

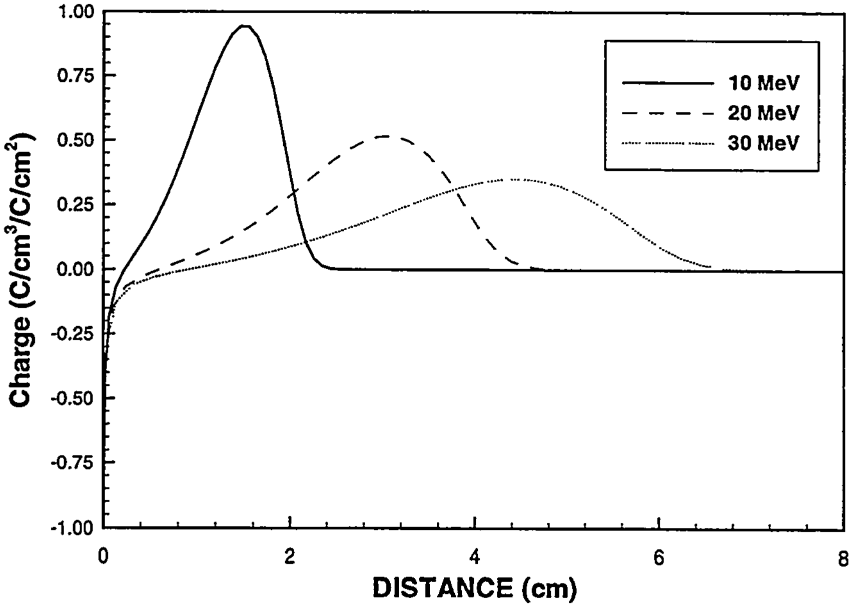

Figure 15: Plot of electron charge deposition as a function of distance in aluminum for 10-, 20-, and 30-MeV electron beams.

3.2 Shielding Calculations

It is important to stop the beam even if you do not need to shield the cables. Having the beam deposit its charge anywhere within the test cell can often be a source of electrical noise. Note that in Figure 13 we used collimators and shields made of aluminum and lead. This is because electrons are far more efficient in making bremsstrahlung in high-Z materials. Photons have much longer ranges than electrons and therefore require much more shielding. The object is not to make an efficient bremsstrahlung converter as shown in Figure 2. Instead of generating bremsstrahlung in the high-Z material and stopping the electrons in the low-Z graphite, which gives little photon attenuation, we want to do just the opposite. Note that, in Figure 15 for the 20-MeV electrons, the charge deposition is zero after ~5 cm; that is, the electron beam is completely stopped. In Figure 14, at ~5 cm the deposition has fallen to a lower value that decreases very slowly at this point. The doses from this depth on are all due to bremsstrahlung. Therefore, a good shield or collimator design for this energy would use 5-cm of aluminum, followed by enough lead to cut the bremsstrahlung dose to the desired level. With this in mind, calculations similar to the photon shielding calculations can be run to determine a shield design for a particular electron spectrum and attenuation.

3.3 Dose in the Dosimeter

The first consideration for the dosimeter is the question of calibration. Although this is not usually an issue for TLDs, it certainly is for PIN diodes. There is a significant possibility that the calibration may be different than that taken at a flash x-ray facility. It is not unusual for some diodes to use high-Z metallizations. Therefore, the issue of dose enhancement should be addressed with calculations and compared to a calibration at the electron-beam facility.

Again, because charged particle equilibrium does not exist in an equilibrium environment, no choice of buffer or equilibrator thickness can create this state. It is often difficult to obtain good agreement with the stopping power because of loss of secondary electrons [19]. Choosing a layer thickness that is equivalent to the device package areal density at least will ensure approximately the same electron spectrum.

Similarly one can use Equation 5 for estimating the silicon free-field dose from the dosimeter response. Using the ratio of stopping powers may give erroneous results, especially at the lower electron energies as discussed in Reference 19.

3.4 Dose in the Device

The procedure is the same as was outlined in the photon section for calculating dose. The only additional work is to examine the charge deposition profile. Try not to have the active region of the device in a region of high charge deposition or erroneous electrical measurements may result.

3.5 Correlation of Dosimeter Dose to Device

The procedure is also the same as was outlined in the photon section, and Equation 6 is still valid. This calculated ratio includes all the effects of attenuation, mass-stopping-power differences, and secondary electron loss. Again, remember that this conversion factor is only good for a particular electron spectrum and geometry. For example, if the thickness of the exit window or a beam scatterer is introduced, you must recalculate the doses in the dosimeter and the device.

The same final calculation is necessary. Using the model of the device, a model of the system chassis and the spectrum and fluence of the working environment, calculate the dose in the device. Compare this with the dose you obtained using Equation 6. If the doses are comparable for all the cross-sections of the device you have modeled, then you are finished. If not, then you have a simulation fidelity problem, and you will have to determine the level of overtest necessary to qualify the component.

4.0 Proton Irradiation

For this example we are going to use the working environment to calculate the shielding effectiveness for an idealized satellite. We cannot use the CEPXS/ONELD code for this problem because it only deals with electrons and photons. The code used for these calculations is the Sandia LITXS/ONELD code [20]. This code has not yet been released to RSICC, but can be obtained from the author. LITXS is similar to CEPXS in that it generates a cross-sections for use in ONELD. However in this case it is for protons instead of photons and electrons. These results are taken directly out of Reference 20.

4.1 Proton Spectrum

Figure 16 shows the integral number spectrum for protons in space for three different environments: 1) a solar flare in an averaged global positioning system (GPS) orbit, 2) a 1 year natural exposure in a 1000 km circular orbit and 60° inclination, and 3) a 1 year natural exposure in a 3000 km circular orbit and 0° inclination.

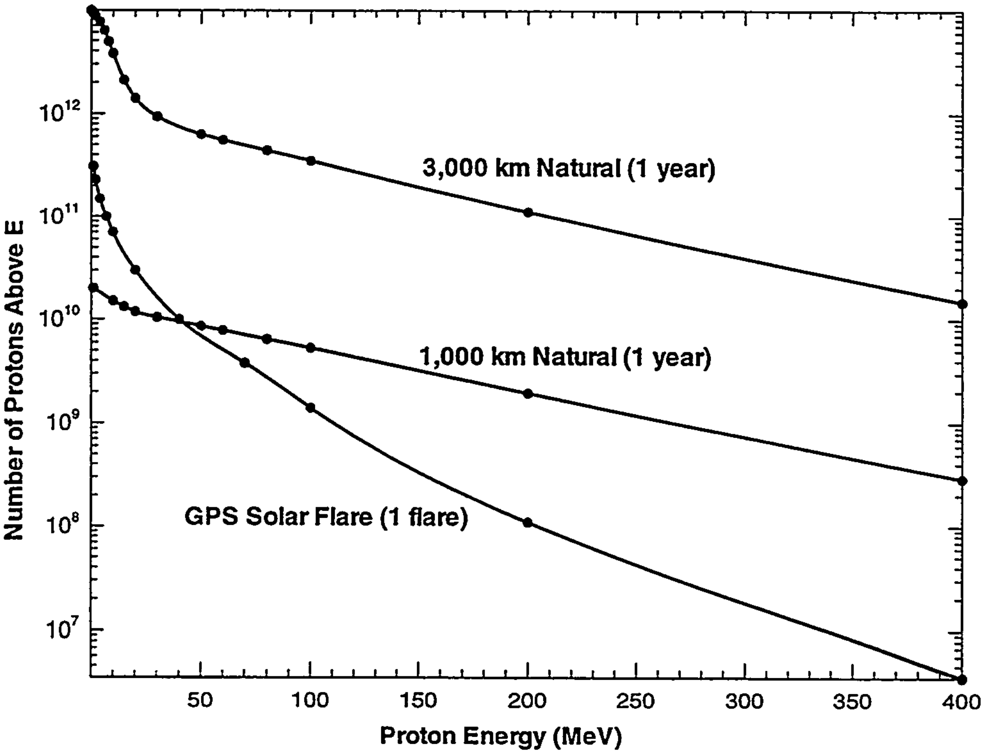

Figure 16: Plot of dose number of protons above an energy versus energy for a solar flare in an averaged GPS orbit, 1 year natural exposure in a 1000 km orbit, and a 1 year natural exposure in a 3000 km orbit.

The first thing you might notice about this integral number spectrum is that it is different than the standard input for ITS or CEPXS/ONELD. Yes, they are both integral number spectra, but Figure 16 integrates "down" and the desired input integrates "up." That is, the input is looking for source particles less than an energy and Figure 16 plots protons greater than an energy.

These can easily be converted using the following equation:

$$IN_{UP} = IN_{MAX} - IN_{DOWN}\,, \tag{7}$$

where IN_{UP} is the number of particles less than an energy, IN_{MAX} is total number of particles, and IN_{DOWN} is the number of particles greater than an energy. Second, it is also apparent that the proton spectrum for the solar flare is much softer (lower average energy) than the natural environments. This difference in energy will affect the choice of shielding.

4.2 Dose in the Device

The effectiveness of a shield can be calculated for an idealized satellite using an isotropic proton source incident upon a spherical-shell shield with an inner radius of 10.0 cm. In this case, I am defining the term isotropic to mean the magnitude of the incident fluence is independent of angle as referenced by the geometry of interest, not with respect to the source itself. This is in essence a 1-D problem that can be calculated by LITXS/ONELD because the only spatial variable is the radius. For consistency we will deal here with only the ionizing dose and not any displacement damage. The results for tantalum and aluminum shells are shown in Figures 17 and 18.

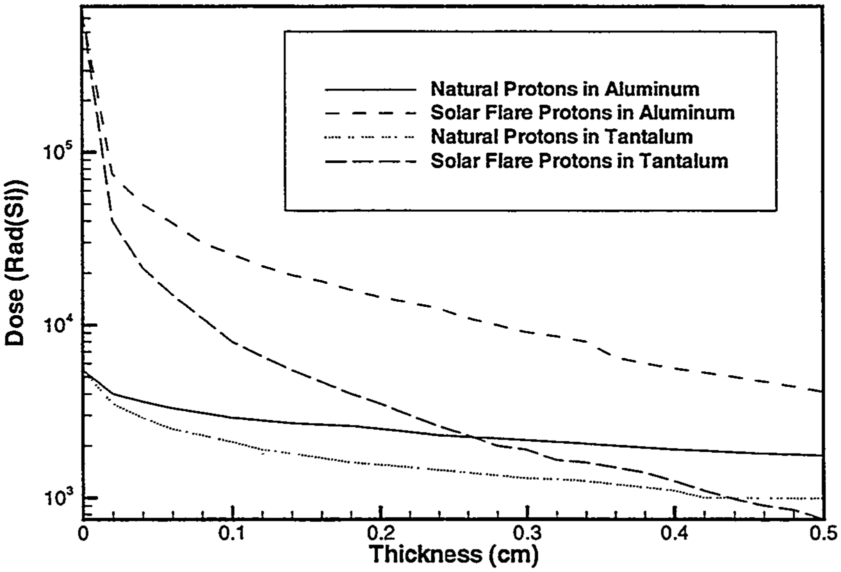

Figure 17: Plot of total ionizing silicon dose at the center of spherical-shell aluminum or tantalum shield as a function of shield thickness in the GPS solar-flare and 1000-km natural proton environments.

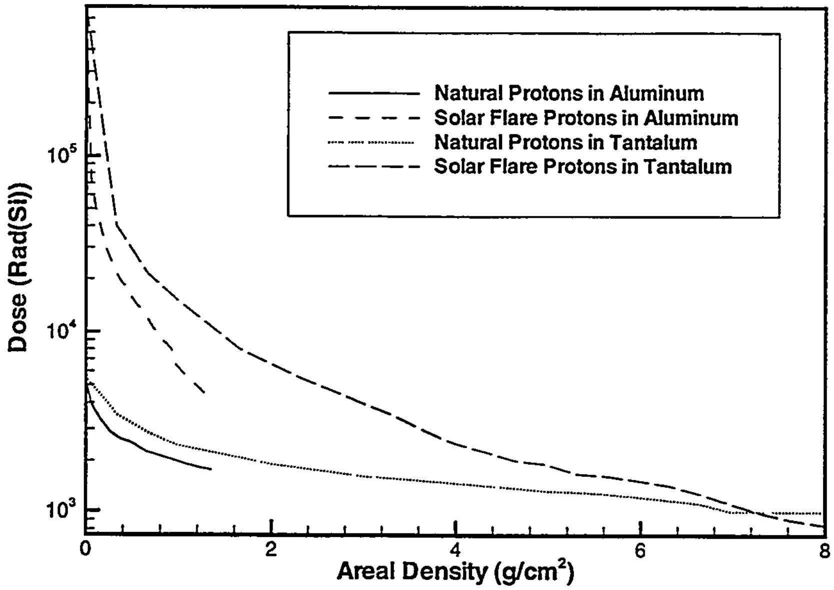

Figure 18: Plot of total ionizing silicon dose at the center of spherical-shell aluminum or tantalum shields as a function of shield areal density in the GPS solar-flare and 1000-km natural proton environments.

In Figure 17 the dose is plotted as a function of thickness of material. From this plot it would appear that the choice of tantalum would be best. If volume were the overriding concern, this would be true. However, mass is usually the quantity of interest. Therefore, Figure 18, which plots the dose as a function of areal density, gives a clearer picture. (Areal density is the thickness multiplied by the density of the material.) From this plot it is clear that the for the same mass, aluminum is the better choice. Again, charged particles transversing high-Z materials generate more radiation than in low-Z materials, especially at lower energies. Note that differences between the shielding effectiveness of tantalum and aluminum are greater for the softer solar flare environment than the natural environment. Also the decrease in dose with thickness or areal density is much greater for the softer spectrum.

4.3 Fluence Normalization

There is a small problem of terminology that needs to be addressed. The fluence, Ψ, used for normalization in most codes is defined to be the number of particles crossing a unit area from one direction. However, the normal omni-directional fluence, Φ, is the sum of particles crossing a point over all directions. In other words, Ψ is a vector quantity and Φ is a scalar quantity. For an isotopic fluence, Ψ is zero, but Φ is not. However, the codes always assume a one way current, that is a source from one side. Therefore one must convert from the one way current normalization to the omni-directional current normalization for comparison to measurements.

For an isotropic fluence,

$$\Phi = \int_0^{4\pi} I d\Omega = 4\pi I , \tag{8}$$

where I is the differential fluence in $d\Omega$ the solid angle Ω, and I is constant, independent of angle, for an isotropic fluence. The one-way current, $\Psi_{2\pi}$, is given by

$$\Psi_{2\pi} = \int_0^{2\pi} d\Omega \left| \vec{e}_j \bullet \vec{e}_\Omega \right| I = \int_0^{2\pi} d\phi \int_0^{\frac{\pi}{2}} d\theta \sin\theta \cos\theta I , \tag{9}$$

where e_j is the unit vector normal to the surface and e_Ω is the unit vector in the direction Ω. Integrating and using Equation 8 we find that

$$\Psi_{2\pi} = \pi I = \frac{\Phi}{4} . \tag{10}$$

Thus, the one-way fluence is one fourth the omni-directional fluence, and the dose in an isotropic fluence is one fourth that calculated by the codes using their fluence normalization.

5.0 Conclusions

This brief overview was designed to give the reader a working knowledge of the terminology, types of radiation transport codes, and relevant problems that can be addressed with them. When used properly for experiment design, the interpretation of the measured results, analysis, and extrapolation to the performance in the working environment can be simplified. Regardless of the particle type, the process of calculating dose in the dosimeter and DUT is the essentially the same. Knowledge of the radiation spectrum and geometry are often the dominant limitation in the accuracy of any radiation transport calculation.

This review is by no means sufficient to use the codes with ease or without error. You are strongly encouraged to study the references contained within this document before attempting to use any radiation transport code.

6.0 Acknowledgments

This work was performed at Sandia National Laboratories and supported by the U. S. Department of Energy under contract DE-AC04-94AL8500. Sandia is a multiprogram laboratory operated by Sandia Corporation, a Lockheed Martin Company, for the U.S. Department of Energy. I also thank W. P. Ballard, C. R. Drumm, D. M Fleetwood, R. P. Kensek, and L. J. Lorence, Jr. for useful discussions and reviews.

7.0 References

[1] L. J. Lorence, Jr., J. E. Morel, and G. D. Valdez, "Users Guide to CEPXS/ONELD: A One-Dimensional Coupled Electron-Photon Discrete Ordinates Code Package, Version 1.0," SAND89-1661, Sandia National Laboratories, September 1989.

[2] Radiation Safety Information Center, Oak Ridge National Laboratory, P.O. Box 2008, Oak Ridge, TN 37821-6362, phone: 423-574-6176, e-mail: pdc@ornl.gov, www:http://epicws.epm.ornl.gov.

[3] R. L. Miller, R. L. Weitz, K. R. Seitz, "A Gamma Spectrometer for AGT/UGT Application," Journal of Radiation Effects, Research and Engineering, Vol. 13, No. 1 p. 16-31, (1996) (ITAR).

[4] A. R. Frederickson, J. T. Bell, and E. A. Beidl, "Analytic Approximation for Charge Current and Deposition by 0.1 to 100 MeV Electrons in Thick Slabs," IEEE Trans. Nuc. Sci. Vol. 42, No. 6, p. 1910-1921, (1995).

[5] L. J. Lorence, Jr., J. E. Morel, and G. D. Valdez, "Results Guide to CEPXS/ONELD: A One-Dimensional Coupled Electron-Photon Discrete Ordinates Code Package, Version 1.0," SAND89-2211, Sandia National Laboratories, July 1990 and references contained within.

[6] PSPICE Users Manual, (MicroSim Corporation, 1986)

[7] DAVINCI 3.0 Users Manual, (Technology Modeling Associates, Inc., 1994)

[8] E 1249, "Standard Practice for Minimizing Dosimetry Errors in Radiation Hardness Testing of Silicon Electronic Devices using Co-60 Sources," American Society for Testing and Materials Standards, Vol. 12.02, Philadelphia, PA, 1996.

[9] E. E. Morris and A. B. Chilton, "Monte Carlo Calculation of the Spectrum of Gamma Radiation form a Collimated Co-60 Source," TRC-68-6, NRDL (1967). Code available from RSICC.

[10] A. R. Frederickson, "Gamma Energy Spectra for the RADC/ES Cobalt 60 Sources," RADC-TR-79-68, Rome Air Development Center, April, 1979.

[11] J. C. Garth, W. L. Chadsey, and R. L. Shepard, "Monte Carlo Analysis of Dose Profiles Near Photon Irradiated Material Interfaces," IEEE Trans. Nuc. Sci., Vol. NS-22, N0. 6, p. 2562-2567 (1975); E. A. Burke and J. C. Garth, "Energy Deposition by Soft X-Rays — An Application to Lithography for VLSI," IEEE Trans. Nuc. Sci., Vol. NS-26, No. 6, p. 4868-4873 (1979); D. M. Long, D. G. Millward, R. L. Fitzwilson, W. L. Chadsey, Handbook for Dose Enhancement Effects in Electronic Devices," RADC-TR-83-84, Rome Air Development Center, March 1983 and many good seminal references contained within; L. D. Posey, T. F. Wrobel, D. C. Evans, W. Beezhold, J. G. Kelly, C. J. MacCallum, F. N. Coppage, T. F. Luera, L. J. Lorence, Jr., "MOS-Transistor Radiation Detectors and X-Ray Dose-Enhancement Effects," IEEE Trans. Nuc. Sci., Vol. NS-33, No. 6, p. 4446-4452 (1985); D. M. Fleetwood, P. S. Winokur, R. W. Beegle, P. V. Dressendorfer, and B. L. Draper, IEEE Trans. Nuc. Sci., Vol. NS-33, No. 6, p. 4369-4375 (1985); D. E. Beutler, D. M. Fleetwood, W. Beezhold, D. Knott, L. J. Lorence, Jr., and B. L. Draper, "Variations in Semiconductor Device Response in a Medium-Energy X-Ray Dose-Enhancing Environment," IEEE Trans. Nuc. Sci., Vol. NS-34, No. 6, p. 1544-1550, (1987); D. M. Fleetwood, D. E. Beutler, L. J. Lorence, Jr., D. B. Brown, B. L. Draper, L. C. Riewe, H. B. Rosenstock, and D. P. Knott, "Comparison of Enhanced Device Response and Predicted X-Ray Dose Enhancement Effects on MOS Oxides," IEEE Trans. Nuc. Sci., Vol. NS-35, No. 6, p. 1265-1271, (1988); D. E. Beutler, W. Beezhold, J. S. Browning, D. M. Fleetwood, N. E. Counts, D. P. Knott, C. L. Freshman, and M. P. Conners, "Comparison of Photocurrent Enhancement and Upset Enhancement in CMOS Devices in a Medium-Energy X-Ray Environment," IEEE Trans. Nuc. Sci., Vol. NS-37, No. 4, p. 1541-1547, (1990).

[12] J. A. Halbleib and T. W. L. Sanford, "Predicted Flash X-Ray Environments Using Standard Converter Configurations," SAND83-2572, Sandia National Laboratories, 1985.

[13] D. E. Beutler, J. A. Halbleib, and D. P. Knott, "Comparison of Experimental Pulse-Height Distributions in Germanium Detectors with Integrated-Tiger-Series-Code Predictions," IEEE Transactions on Nuclear Science, Vol. NS-36, No. 6, p. 1912-1919, (1989); R. W. Tallon, D. C. Koller, R. M. Pelzl, R. D. Pugh, R. D. Bellem, "5 to 160 keV Continuous-Wave X-Ray Spectral Energy Distribution and Energy Flux Density Measurements," IEEE Trans. Nuc. Sci. NS-41, No. 6, p. 2112-2117 (1994); R. D. Bellem, K. L. Critchfield, R. M. Pelzl, R. D. Pugh, R. W. Tallon, "Analytical and Experimental Dosimetry Techniques for Calibrating a Low Energy X-Ray Radiation Source," IEEE Trans. Nuc. Sci. NS-41, No. 6, p. 2139-2146 (1994)

[14] G. A. Carlson and L. J. Lorence, "A Differential Absorption Spectrometer for Determining Flash X-Ray Spectra from 10 to 2000 keV," IEEE Transactions on Nuclear Science, Vol. NS-35, No. 6, p. 1255-1259 (1988); G. A. Carlson, D. E. Beutler, K. D Seager, and D. P. Knott, "Comparison of Measured Responses in Two Spectrally-Sensitive X-Ray Detectors to Predictions Obtained using the ITS Radiation Transport Code," IEEE Transactions on Nuclear Science, Vol. NS-35, No. 6, p. 1272-1277 (1988).

[15] E 665, "Standard Practice for Determining Absorbed Dose Versus Depth in Materials Exposed to the X-Ray Output of Flash X-ray Machines," American Society for Testing and Materials Standards, Vol. 12.02, Philadelphia, PA, 1996.

[16] Y. S. Horowitz, "Thermoluminescence and Thermoluminescent Dosimetry," CRC Press, Inc. Boca Raton, Florida, 1984; ICRU Report 34, "The Dosimetry of Pulsed Radiation,"Internaltional Commission on Radiation Units and Measurements, Bethesda, MD, 1982.

[17] E 668, "Standard Practice for Application of Thermoluminescence-Dosimetry (TLD) Systems for Determining Absorbed Dose in Radiation-Hardness Testing of Electronic Devices," American Society for Testing and Materials Standards, Vol. 12.02, Philadelphia, PA, 1996.

[18] D. E. Beutler, J. A. Halbleib, T. W. L. Sanford, D. L. Fehl, and D. P. Knott, "Dosimetry Considerations for the High-Energy Photon/Electron Environment of HERMES III: Implications for Experiments and Modeling," IEEE Transactions on Nuclear Science, Vol. NS-38, No. 6, p. 1736-1745 (1991); T. W. L. Sanford, D. E. Beutler, J. A. Halbleib, and D. P. Knott, "Experimental Verification of Bremsstrahlung Production and Dosimetry Predictions for 15.5 MeV Electrons," IEEE Transactions on Nuclear Science, Vol. NS-38, No. 6, p. 1160-1170 (1991).

[19] D. E. Beutler, L. J. Lorence, Jr., and D. B. Brown, "Dosimetry in Linac Electron-Beam Environments," IEEE Transactions on Nuclear Science, Vol. NS-38, No. 6, p. 1171-1179 (1991).

[20] C. R. Drumm, "Proton Transport Methods for Satellite Shield Modeling," SAND93-0200, Sandia National Laboratories, 1993

DISTRIBUTION

50	MS 1179	D. E. Beutler, 9341
50	1179	L. J. Lorence, Jr., 9341
1	9018	Central Technical Files, 8940-2
5	0899	Technical Library, 4916
2	0619	Review & Approval Desk, 12690 For DOE/OSTI